

**Centro de Investigación y de Estudios Avanzados
del
Instituto Politécnico Nacional**

DEPARTAMENTO DE FÍSICA

**Una primera aproximación a la identificación
de muones con el sistema de PMTs de ICARUS**

Tesis que presenta

Aldo Castro Fernández

para obtener el Grado de

Maestro en Ciencias

en la Especialidad de

Física

Directores de tesis:

**Dr. Omar Gustavo Miranda Romagnoli
Dra. Minerba Betancourt**



**CENTRO DE INVESTIGACION Y DE ESTUDIOS AVANZADOS
DEL INSTITUTO POLITECNICO NACIONAL**

PHYSICS DEPARTMENT

**“First attempt for a muon identification with
ICARUS PMT system”**

Thesis submitted by

Aldo Castro Fernández

In order to obtain the

Master of Science

degree, speciality in

Physics

Supervisors:

**Dr. Omar Gustavo Miranda Romagnoli
Dra. Minerba Betancourt**

Mexico City

November, 2021.

Acknowledgements

I would like to express my deepest appreciation to my supervisors Dr. Omar Miranda and Dra. Minerba Betancourt for their support and patience during the development of this project. Also, I do like to recognize the help and suggestions that I received from Guadalupe Moreno, Animesh Chatterjee, and the committee formed by Dr. Luis Manuel and Dr. Ricardo López.

Many thanks to my friends and family for believing in me. I would especially like to extend my deepest gratitude to my mom Esmeralda and grandparents Francisco and Lety for their unconditional care and support.

Finally, thanks to Consejo Nacional de Ciencia y Tecnología, CONACyT for having supported me with the fellowship in this posgrate. In the same way, I thank the CONACyT project A1-S-23238.

Abstract

First attempt for muon identification with ICARUS PMT system.

by

Aldo Castro Fernández
Master Thesis. CINVESTAV

ICARUS is an experiment that will measure neutrino interactions through a liquid-argon detector. It uses time projection chambers and also a certain number of photomultiplier tubes (PMT). In this thesis, we develop a first attempt to identify muons in the detector by using the PMTs. We will show preliminary results on the development of this algorithm and discuss possible directions to develop a tool that can be used in the future for this muon identification. Different additional tools and experimental details that were needed to elaborate this work are also presented.

Resumen

Una primera aproximación a la identificación de muones con el sistema de PMTs de ICARUS.

por

Aldo Castro Fernández

Tesis de Maestría. Departamento de Física, CINVESTAV

ICARUS es un experimento que medirá interacciones de neutrinos usando un detector de argón líquido. ICARUS usa cámaras de proyección temporal y también un cierto número de tubos fotomultiplicadores (PMT por sus siglas en inglés). En esta tesis exponemos un primer intento de identificar muones en este detector usando los PMTs. Mostramos resultados preliminares en el desarrollo de este algoritmo y discutimos posibles formas de desarrollar una herramienta que pueda ser usada en el futuro para dicha identificación de muones. Se presentan también diversas herramientas adicionales y detalles experimentales que fueron necesarios para elaborar este trabajo.

Contents

Acknowledgements	I
Abstract	II
Resumen	III
List of Tables	VI
List of Figures	VIII
1 Introduction	1
1.1 The Standard Model	1
2 Neutrino Oscillations	5
2.1 Standard Derivation of the Neutrino Oscillation Probability.	6
2.2 Neutrino Oscillation Experiments	10
2.3 The Experimental Anomalies	14
3 ICARUS in Short Baseline Neutrino Program Fermilab.	16
3.1 Short Baseline Neutrino Program.	16
3.2 Micro Booster Neutrino Experiment.	17
3.3 Short Baseline Near Detector.	18
3.4 Booster Neutrino Beam (BNB) and Neutrinos at the Main Injector (NuMI).	18
4 Design of ICARUS detector.	21

4.1	A new concept for neutrino detectors.	21
4.2	ICARUS T600 Detector Overview.	23
4.3	Description and operation of LAr-TPCs in ICARUS detector.	24
4.4	The internal PMT system	30
5	Muon Tracking	33
5.1	Optical Model	33
5.2	Muon Simulation with LArSoft	38
6	Conclusion and Perspectives	44
	References	47

List of Tables

1.1	Types of interaction filed.	2
1.2	Fermions are divided into two categories leptons and quark which in turn are divided into generations.	2
1.3	Mass and charge of fermions [1]. The charge is given in units of elementary charge e .	3
2.1	Types of neutrino oscillation experiments.	14
2.2	Short Baseline Neutrino Anomalies.	15
3.1	BNB neutrino production. The corresponding decays of the negative particles are the charge conjugates listed here [2].	20
4.1	MC calculations of expected event rates in ICARUS-T600.	29
4.2	Summary of Scanning Efforts ICARUS 2021. In all runs the trigger was MinBias except for run 6105 where it was Majority 5.	29

List of Figures

3.1	View of the Short-Baseline Neutrino experimental area at Fermilab. (https://sbn.fnal.gov/)	17
3.2	A schematic view of the MicroBooNE detector. In the right-hand image are shown the three wire planes of the TPC, the PMTs (not shown) are located behind the wires. Image from [3].	18
3.3	The Short-Baseline Near Detector (SBND). Image from https://sbn-nd.fnal.gov/	19
3.4	Four particle accelerators and storage rings comprises the Fermilab accelerator complex. Image from https://www.fnal.gov/pub/science/particle-accelerators/accelerator-complex.html	19
4.1	ICARUS T600 detector schematics, showing both modules and the common insulation surrounding the detector; inner structures and feed-through's are also shown. On the bottom a view of the detectors is presented with the wire chambers and the high voltage system (race-tracks and cathodes). Image from [4].	23
4.2	The three wire planes of a TPC installed in the T600 detector.	25
4.3	Scintillation and ionization mechanism of liquid argon. Image from [5].	26
4.4	The electric field generated between the cathode and the anode (wire planes) acts on the electrons, leading them to the wire planes, where a signal is obtained when interacting with each wire plane, which will later be used in the reconstruction of the event. Image from [6].	26
4.5	Event 1166, ν_μ -candidate.	27
4.6	Event 1166, ν_μ -candidate. Induction-2 (View U).	28
4.7	Scheme of 9357 FLA Electron Tubes PMTs.	30

4.8	PMT visible behind the three wire planes.	31
4.9	PMTs placed in one of the ICARUS TPCs. Image from: https://icarus.fnal.gov/	32
5.1	Schematic of the optical model that predicts the First Hit Time of the ICARUS PMTs. A muon is shown traveling through cryostat 0 east. \vec{R}_i is the position of the i th PMT, \vec{R}_0 is the injecting position of the muon track into the LAr, \hat{V} is the direction of the muon track, ΔR is the distance between the PMTs that turn on, $\ell_{i,j}$ is the distance between the emission points of the photons, and θ is the Cherenkov angle.	34
5.2	Top view of Cryostat-1-East illustrating the geometry used in ICARUS to calculate the variable $\ell_{i,j}$	35
5.3	Muon simulated using LArSoft, has an energy of 2GeV, and is perpendicular to Induction 1.	38
5.4	PMTs On in the simulated muon.	39
5.5	Histogram of the Monte Carlo data from the simulated muon FHT.	40
5.6	FHT in the PMTs on the plane located at $x = -59.36$ cm.	40
5.7	FHT in the PMTs on the plane located at $x = -381.07$ cm.	41
5.8	Points that represent the position of the possible Ro for the event.	41
5.9	χ^2 vs \vec{R}_{0x} . The sample was a muon with an energy of 2GeV with an angle of 0° with respect to the Z axis. $\vec{R}_{0x} = -275$ cm is the predicted value.	42
5.10	χ^2 vs \vec{R}_{0y} . $\vec{R}_{0y} = -71$ cm is the predicted value.	42
5.11	χ^2 vs \vec{R}_{0z} . $\vec{R}_{0z} = -785$ cm is the predicted value.	43
6.1	Optical Model in the case of $\ell = 0$	45

Chapter 1

Introduction

1.1 The Standard Model

The Standard Model of elementary particles responds to one of the most ambitious questions that man has asked. What is the world made of?. In this model, formulated in the 1970s, the Universe content is made out of two kinds of elementary particles: fermions, and bosons. This model also gives a mathematical structure to their interactions.

The physical equations that describe elementary particles must remain unchanged under Lorentz transformations. Therefore, the Standard Model provides a mathematical structure guided by principles of symmetry. The symmetry is provided by group theory, $SU(3)_C \times SU(2)_L \times U(1)_Y$, where subscripts represent color "C", left-handed chirality "L", and weak hypercharge "Y".

The electroweak model is a physical theory that is part of the Standard Model. It is based on the symmetry group $SU(2)_L \times U(1)_Y$ and unifies the weak interaction and electromagnetism. The symmetry under the color group $SU(3)_C$ is studied by the quantum chromodynamics (QCD), the theory of strong interactions. Compared with the scale for particle physics experiments, the gravitational interaction is much weaker than the others, e.g., the gravitational potential between two protons is roughly 10^{-39} times weaker than the Coulomb potential between them [7]. Gravitational forces can be neglected to a very good approximation. A quantum theory of gravitation is not universally accepted. It is supposedly mediated by the exchange of a spin 2 boson, the graviton. Currently, there are experiments to detect gravitons [8]. Table 1.1 lists the four types of interaction fields in nature.

The classification of fundamental particles into fermions and bosons is due to

Interaction field	Mediator	Spin
Strong field	gluon, G	1
Electromagnetic field	photon, γ	1
Weak field	W^\pm, Z^0	1,1
Gravitational field	"Graviton" postulated	2

Table 1.1: Types of interaction field.

	$1^{st} generation$	$2^{nd} generation$	$3^{rd} generation$
Leptons	electron neutrino, ν_e electron, e	muon neutrino, ν_μ muon, μ	tau neutrino, ν_τ tau, τ
Quarks	up, u down, d	charm, c strange, s	top t bottom, b

Table 1.2: Fermions are divided into two categories leptons and quark which in turn are divided into generations.

the type of statistics they obey. If the particle has a half-integral spin, it is called fermion. It follows the Fermi-Dirac statistic, while if it has an integral spin, it is called boson, obeying the statistic of Bose-Einstein.

There are two fermion categories, leptons, and quarks listed in Table 1.2 which in turn are divided into generations. Each generation of leptons is divided into a lepton with electrical charge -1 and a neutral lepton (e.g., $1^{st} generation$: e and ν_e). In comparison, quarks can be divided into those with charge $+\frac{2}{3}$ and those with charge $-\frac{1}{3}$ (e.g., $1^{st} generation$: u and d). The members of the 3^{rd} generation have masses greater than the members of the previous generations, in the same way, the 2^{nd} generation has more mass than the 1^{st} generation. The existence of three generations is a puzzling feature. The fact that each generation of fermions differs only by the mass of the particles while the other properties are identical is something that the standard model does not explain. The masses and electric charges of fermions are given in Table 1.3.

We distinguish leptons and quarks because quarks participate in all the interactions, whereas leptons do not participate in interactions. Quarks do not exist as free particles, and they always appear in bounded states called hadrons. An isolated quark has never been observed. There are six types of quarks to understand the properties of hadrons: "up" (u), "down" (d), "charm" (c), "strange" (s), "top" (t), and "bottom" (b). The *mesons* are the most simple quark systems composed of a quark-antiquark state, while *baryons* are particles made up of three quarks. The proton and neutron are examples of baryons made up of two u quarks and one d

Lepton	Mass	Charge	Quark	Mass	Charge
e	0.510 MeV	-1	u	$1.5 - 4$ MeV	$+2/3$
ν_e	< 15 eV	0	d	$4 - 8$ MeV	$-1/3$
μ	105.65 MeV	-1	c	$1.15 - 1.35$ GeV	$+2/3$
ν_μ	< 190 keV	0	s	$80 - 130$ MeV	$-1/3$
τ	1.777 GeV	-1	t	174.3 ± 5.1 GeV	$+2/3$
ν_τ	< 18.2 MeV	0	b	$4.1 - 4.4$ GeV	$-1/3$

Table 1.3: Mass and charge of fermions [1]. The charge is given in units of elementary charge e .

quark (uud) and two d and one u (ddu), respectively. The proton is the only stable baryon. All mesons are unstable. Since quarks are always found as hadron components, their masses do not have the usual classical meaning, and their meaning depends on how the masses are defined. In Table 1.3, the masses of the quarks are called current masses, which are parameters in the standard model [1].

The first elementary particle discovered was the electron, e , in 1897 by J.J. Thomson. The muon, μ , was discovered in 1936 as a component of the cosmic radiation "showers" by Carl D. Anderson and Seth Neddermeyer [9]. Finally, the τ lepton was discovered by a group led by Martin Perl at the Stanford Linear Accelerator Center in California in 1975 [10]. Muon μ and tau τ are said to be heavier unstable versions of the electron, being heavier, can decay into lighter particles, which electron cannot. Another difference is the lifetimes of muon and tau since they have a finite value, while the electron is considered a stable particle that does not decay. The electron is the least massive particle with a nonzero electric charge, so its decay would violate the charge conservation [11].

Wolfgang Pauli proposed the existence of the neutrino in 1930, to explain the continuous spectrum of electrons in nuclear beta decay. The Reines-Cowan neutrino experiment confirmed its existence in 1956 [12]. Neutrinos ν_α have a "flavor" for each charged lepton ℓ_α : $\alpha = e, \mu, \tau$. The electron neutrino ν_e is so named because it is related to the beta decay where an electron is emitted. The muon, μ , is also accompanied by its neutrino, ν_μ . It was discovered in 1962 in the Brookhaven experiment of Lederman, Schwartz [13], through the decay of the meson pion $\pi \rightarrow \mu + \nu_\mu$. Finally, when tau lepton, τ , was found, the existence of ν_τ was immediately deduced. The discovery of the tau neutrino ν_τ was announced in July 2000 in the DONUT (Direct Observation of the NU Tau) collaboration of Fermilab [14].

Neutrinos are neutral particles that do not interact electromagnetically but do interact through weak interactions. In the standard model, neutrinos are considered

massless. By observing the neutrino flavor change, current experiments [15] indicate that neutrinos have a non-zero mass, as will be discussed in Chapter 2.

Chapter 2

Neutrino Oscillations

Beyond the standard model, neutrinos have a very small mass that produces oscillations between the different neutrino flavors. To model these oscillations, Pontecorvo introduced the concept of the sterile neutrino, a neutral fermion that does not participate in weak interactions. From the discovery of the muon neutrino ν_μ , Pontecorvo predicted the Solar Neutrino Problem [16] as consequence of $\nu_e \rightarrow \nu_\mu$ (or $\nu_e \rightarrow \nu_{sterile}$) transitions even before the first measurement of the solar electron neutrino flux in the Homestake experiment [17].

Pontecorvo in the deduction of the probability of neutrino oscillations was based analogously on kaon oscillations [18, 19], however, the results were not satisfactory. Finally, Eliezer and Swift [20], Fritzsch and Minkowski [21] developed the development of the standard theory of oscillations in the plane wave approximation, and Bilenky and Pontecorvo [22].

For the derivation of the probability of neutrino oscillations, in addition to considering neutrinos as particles with mass, it is important to consider that they are also relativistic particles. Neutrino masses are smaller than about 1eV and only neutrinos with energy greater than 100 keV can be detected. Neutrinos are detected in two different types of processes.

- Charged-current or neutral-current weak scattering processes:
 - In charged-current (CC) weak interaction processes, neutrinos ν_α are produced from a charged leptons ℓ_α^- (e^- , τ^- , μ^-), e.g. they are produced in the transitions $\ell_\alpha^- \rightarrow \nu_\alpha$ or creation of $\ell_\alpha^+ \nu_\alpha$ pair.
 - In neutral current (NC) weak interaction process neutrinos can also generated $e^- e^+ \rightarrow \nu + \bar{\nu}$, in this case the neutrinos do not have a definite flavor, giving rise to oscillations between active and sterile neutrinos [23].

- Elastic scattering process $\nu + e^- \rightarrow \nu + e^-$, process used in the Super-Kamiokande solar neutrino experiment [24].

2.1 Standard Derivation of the Neutrino Oscillation Probability.

Neutrinos come in three flavors associated with weak interactions to the charged leptons: electron e , muon μ , or tau τ . Each associated flavor corresponds to an antiparticle called an antineutrino. The Standard Model theory states that neutrinos are fermions with spin 1/2, chargeless, massless, and only experiment weak interactions.

It has been observed that neutrinos can change their flavors during their travel [24]. That is if a neutrino is generated with a certain flavor, and we detected after traveling some distance, we could find it with a different flavor.

For the derivation of the standard theory of neutrino oscillations, a neutrino with flavor α and momentum \vec{p} , created in a charged-current interaction of a lepton ℓ_α^- or together an antilepton ℓ_α^+ , is described by the flavor state

$$|\nu_\alpha\rangle = \sum_k U_{\alpha k}^* |\nu_k\rangle \quad (\alpha = e, \mu, \tau), \quad (2.1)$$

where $U_{\alpha k}^*$ is called leptonic mixing matrix, and its presence of weight in the state $|\nu_i\rangle$, in the flavor state $|\nu_\alpha\rangle$, it is due to the superposition of massive neutrinos generated by the leptonic charged current, which contain creation operators of massive neutrino.

We consider a finite normalization volume V , where V is the volume of a cube with side L , with periodic conditions at the boundaries (the momentum is quantized at the boundaries), to have orthonormal massive neutrino states

$$\langle \nu_k | \nu_j \rangle = \delta_{kj}, \quad (2.2)$$

flavor states are also orthonormal, due to the unitarity of the mixing matrix

$$\langle \nu_\alpha | \nu_\beta \rangle = \sum_{kk'} \langle \nu_k | U_{\alpha k} U_{\beta k'}^* | \nu_{k'} \rangle \quad (2.3)$$

$$= \sum_{kk'} U_{\alpha k} U_{\beta k'}^* \delta_{kk'} \quad (2.4)$$

$$= \sum_k U_{\alpha k} U_{\beta k}^* \quad (2.5)$$

$$= \delta_{\alpha\beta}. \quad (2.6)$$

We notice in Eq. (2.5) the unitarity of the mixing matrix, that is

$$U^\dagger U = I \quad \text{or} \quad U U^\dagger = I \quad (2.7)$$

$$\sum_\alpha U_{\alpha k}^* U_{\alpha j} = \delta_{kj} \quad \text{or} \quad \sum_k U_{\alpha k} U_{\beta k}^* = \delta_{\alpha\beta}. \quad (2.8)$$

We study the evolution in time of massive neutrino states. These are eigenstates of the Hamiltonian

$$\hat{H} |\nu_k\rangle = E_k |\nu_k\rangle, \quad (2.9)$$

the system is an ultrarelativistic neutrino, so the energy eigenvalues are

$$E_k = \sqrt{\vec{p}^2 + m_k^2}. \quad (2.10)$$

The Schrödinger equation

$$i \frac{d}{dt} |\nu_k\rangle = \hat{H} |\nu_k\rangle, \quad (2.11)$$

tells us that the massive neutrino states evolve in time as plane waves

$$|\nu_k(t)\rangle = e^{-iE_k t} |\nu_k\rangle, \quad (2.12)$$

a neutrino created with a definite flavor α at time $t = 0$ is described by Eq. (2.1), substituting Eq. (2.12) in Eq. (2.1) we find the evolution of the flavor states

$$|\nu_\alpha(t)\rangle = \sum_k U_{\alpha k}^* e^{-iE_k t} |\nu_k\rangle \quad (2.13)$$

such that

$$|\nu_\alpha(t=0)\rangle = |\nu_\alpha\rangle \quad (2.14)$$

To express the massive states in terms of the flavor states we invert the relation (2.1) using the unitarity relation Eq. (2.8)

$$\sum_{\alpha} U_{\alpha j} |\nu_{\alpha}\rangle = \sum_{\alpha} \sum_k U_{\alpha j} U_{\alpha k}^* |\nu_k\rangle, \quad (2.15)$$

$$\sum_{\alpha} U_{\alpha j} |\nu_{\alpha}\rangle = \sum_j \delta_{kj} |\nu_k\rangle, \quad (2.16)$$

$$\Rightarrow |\nu_k\rangle = \sum_{\alpha} U_{\alpha k} |\nu_{\alpha}\rangle. \quad (2.17)$$

substituting Eq. (2.17) in Eq. (2.13) we have

$$|\nu_{\alpha}(t)\rangle = \sum_{\beta} \sum_k (U_{\alpha k}^* e^{-iE_k t} U_{\beta k}) |\nu_{\beta}\rangle, \quad \beta = e, \tau, \mu. \quad (2.18)$$

the last equation indicates that the pure flavor state Eq. (2.1) at $t = 0$, becomes a superposition of different flavor states at $t > 0$ if the mixing matrix is not diagonal.

The amplitude of transitions $\nu_{\alpha} \rightarrow \nu_{\beta}$ as a function of time is

$$A_{\nu_{\alpha} \rightarrow \nu_{\beta}}(t) = \langle \nu_{\alpha} | \nu_{\beta}(t) \rangle = \sum_k U_{\alpha k}^* U_{\beta k} e^{-iE_k t}, \quad (2.19)$$

the transition probability is given by

$$P_{\nu_{\alpha} \rightarrow \nu_{\beta}}(t) = |A_{\nu_{\alpha} \rightarrow \nu_{\beta}}(t)|^2 = \sum_{k,j} U_{\alpha k}^* U_{\beta k} U_{\alpha j} U_{\beta j}^* e^{-i(E_k - E_j)t}, \quad (2.20)$$

The dispersion relation for ultrarelativistic neutrinos can be approximated by

$$E_k = \sqrt{\vec{p}^2 + m_k^2} \approx |\vec{p}| + \frac{m_k^2}{2|\vec{p}|} + \dots \quad (2.21)$$

with

$$E = |\vec{p}| \quad (2.22)$$

is the neutrino energy, neglecting the mass contribution. Then the exponential of Eq. (2.28) can be write as

$$E_k - E_j \approx \frac{m_k^2 - m_j^2}{2E} = \frac{\Delta m_{kj}^2}{2E}. \quad (2.23)$$

Substituting in Eq. (2.28) the transition probability can be approximated by

$$P_{\alpha \rightarrow \beta}(t) = |A_{\alpha \rightarrow \beta}(t)|^2 = \sum_{k,j} U_{\alpha k}^* U_{\beta k} U_{\alpha j} U_{\beta j}^* \exp\left(\frac{-i\Delta m_{kj}^2 t}{2E}\right), \quad (2.24)$$

in neutrino oscillation experiments the propagation time is not measured but the distance L between the source and the detector is known (in fact the distance L characterizes the different types of neutrino oscillations experiments as will be seen in the following sections). Since neutrinos propagate almost at the speed of light, the approximation $t = L$ is possible. The phases of neutrino oscillations is

$$\Phi_{kj} = -\frac{\Delta m_{kj}^2 L}{2E}. \quad (2.25)$$

Experiments determines the quantities L and E and the squared-mass differences Δm_{kj}^2 are physical constants. The elements of the mixing matrix U specifies the amplitude of the oscillations. Then measurements of neutrino oscillations allow to know information about the squared-mass differences Δm_{kj}^2 and the elements of the mixing matrix U .

Two-neutrino mixing

Two-neutrino mixing is a useful approximation in which only two massive neutrinos are considered. Its usefulness lies in the oscillation formulas, the two-neutrino mixing equations are much simpler and depend on fewer parameters than in the case of three-neutrino mixing. Moreover, the experiments are not sensitive to the influence of three-neutrino mixing, the data can be analyzed by using an effective model with two-neutrino mixing.

The approximation to two neutrinos, consider two flavor neutrinos ν_α and ν_β , which can be any two flavors of the three that exist, or a linear combination of these. The case of experiments of electron neutrino disappearance is given by a linear combination: $\nu_\alpha = \nu_e$ and $\nu_\beta = c_{\mu\nu}\nu_{\mu\nu} + c_{\tau\tau}\nu_{\tau\tau}$, with $c_\mu^2 + c_\tau^2 = 1$. The two flavor neutrino states are linear superpositions of the two massive neutrinos ν_1 and ν_2 with coefficients given by the elements of the two-neutrino effective mixing matrix

$$U = \begin{pmatrix} \cos \vartheta & \sin \vartheta \\ -\sin \vartheta & \cos \vartheta \end{pmatrix}, \quad (2.26)$$

ϑ is the mixing angle, with a value in the interval $0 \leq \vartheta \leq \pi/2$. In this approximation there is only one squared-mass difference:

$$\Delta m^2 \equiv \Delta m_{21}^2 \equiv m_2^2 - m_1^2. \quad (2.27)$$

m_1 is defined as the lightest muon, so that Δm is positive. The expression for the probability of $\nu_\alpha \rightarrow \nu_\beta$ transitions with $\alpha \neq \beta$ can be derive from Eq. (2.24)

$$P_{\alpha \rightarrow \beta}(L, E) = \frac{1}{2} \sin^2 2\vartheta [1 - \cos(\frac{\Delta m^2 L}{2E})] \quad (2.28)$$

or,

$$P_{\alpha \rightarrow \beta}(L, E) = \frac{1}{2} \sin^2 2\vartheta \sin^2(\frac{\Delta m^2 L}{2E}) \quad (2.29)$$

The survival probability is called the case $\alpha = \beta$, $P_{\alpha \rightarrow \alpha}(L, E)$ easily obtained by unitarity form the transition probability in Eq. (2.29)

$$P_{\alpha \rightarrow \alpha}(L, E) = 1 - P_{\alpha \rightarrow \beta}(L, E) = 1 - \sin^2 2\vartheta \sin^2(\frac{\Delta m^2 L}{2E}) \quad (2.30)$$

Due to the spatial resolution of the source and detector in experiments (i.e. the source has an energy spectrum and the energy resolution of the detector is finite.), it is practically impossible to measure the oscillation probabilities for precise values of the neutrino propagation distance L and the neutrino energy E . Therefore, it is always necessary to average the oscillation probability over the appropriate distributions of the distance L and the energy E . In the case of two-neutrino mixing, the transition probability measured in practice is obtained by averaging the cosine function in Eq. (2.28) over the appropriate distribution $\Phi(L/E)$ of L/E

$$\langle P_{\alpha \rightarrow \beta}(L, E) \rangle = \frac{1}{2} \sin^2 2\vartheta [1 - \langle \cos(\frac{\Delta m^2 L}{2E}) \rangle], \quad (2.31)$$

with

$$\langle \cos(\frac{\Delta m^2 L}{2E}) \rangle = \int \cos(\frac{\Delta m^2 L}{2E}) \Phi(\frac{L}{E}) d(\frac{L}{E}). \quad (2.32)$$

2.2 Neutrino Oscillation Experiments

Neutrino oscillation experiments are divided into, "Appearance experiments" and "Disappearance experiments". The Appearance experiments measure the transitions between different neutrino flavors. In this case, the experiment is sensitive to rather small values of the mixing angle. In the case of Disappearance experiments, the survival probability of a neutrino flavor is measured by counting the number of interactions in the detector and comparing it with the expected one. In this type of experiment, it is hard to measure small values of the mixing angle.

In the case of two-neutrino mixing, it should be noted that transitions to different flavors cannot be measured if

$$\frac{\Delta m^2 L}{2E} \ll 1. \quad (2.33)$$

And if

$$\frac{\Delta m^2 L}{2E} \gg 1 \quad (2.34)$$

the average transition probability is observable, yielding information only on $\sin 2\vartheta^2$.

We can design an experiment sensitive to Δm^2 , since it remains fixed and with a right choice of values of the ratio $\frac{L}{E}$, then we say that an experiment is sensitive to Δm^2 when

$$\frac{\Delta m^2 L}{2E} \approx 1 \quad (2.35)$$

the experiments are classified by its average value of the ratio $\frac{L}{E}$, which determines its sensitivity to Δm^2 .

Types of neutrino oscillation experiments.

Short BaseLine experiments (SBL):

- Reactor SBL. In this type of experiments the range of the ratio $\frac{L}{E}$ and the sensitivity to $\Delta m^2 \geq 0.1 \text{eV}^2$ are:

$$\frac{L}{E} \leq \frac{10 \text{m}}{\text{MeV}} \Rightarrow \Delta m^2 \geq 0.1 \text{eV}^2 \quad (2.36)$$

and utilize large isotropic fluxes of electron antineutrinos produced in nuclear reactors.

- Accelerator SBL. These are experiments with beams of neutrinos produced by decay of different particles:
 - Pion Decay In Flight (DIF). This beam is composed mainly of muon neutrinos produced by the decay of pions and kaons, initially produced by a beam of protons striking a target. The typical energy of the neutrinos is of the order of a few GeV and the distance L of 1 km, giving a sensitivity of:

$$\frac{L}{E} \leq \frac{1 \text{km}}{\text{GeV}} \Rightarrow \Delta m^2 \geq 1 \text{eV}^2. \quad (2.37)$$

- Muon Decay At Rest (DAR). This beam is composed of muon antineutrinos coming from the decay muon decay $\mu^+ \rightarrow e^+ + \nu_e + \bar{\nu}_\mu$, produced in the pion decay $\pi^+ \rightarrow \mu^+ + \nu_\mu$ and stopped in the target. The distance L is of several tens of meters, giving a sensitivity of:

$$\frac{L}{E} \leq \frac{1m}{MeV} \Rightarrow \Delta m^2 \geq 1eV^2. \quad (2.38)$$

This is one of the lowest energy experiments.

- Beam Dump. In this case, a proton beam with energy of the order of some hundreds of GeV is completely stopped in a thick target, called the beam dump, the proton nucleon interactions generate heavy hadrons, which decay promptly emitting fluxes of electron and muon neutrinos with energies of the order of 10^2 GeV. The distance L is the order of 1 km giving a sensitivity of:

$$\frac{L}{E} \leq \frac{10^{-2}m}{MeV} \Rightarrow \Delta m^2 \geq 10^2 eV^2. \quad (2.39)$$

Long Base Line Experiments (LBL) have sources similar to SBL experiments, but the source–detector distance is about two or three orders of magnitude larger:

- Reactor LBL are reactor neutrino experiments in which the source–detector distance is of the order of $1km$. The range of L/E covered by these experiments and their sensitivity to Δm^2 are

$$\frac{L}{E} \leq \frac{10^3m}{MeV} \Rightarrow \Delta m^2 \geq 10^{-3}eV^2 \quad (2.40)$$

- Accelerator LBL is neutrino experiments with a muon neutrino or antineutrino beam produced by DIF created by shooting a proton beam to a target. The source–detector distance is about 10^2 – 10^3km , leading to a range of L/E and a sensitivity to Δm^2 given by

$$\frac{L}{E} \leq \frac{10^3km}{GeV} \Rightarrow \Delta m^2 \geq 10^{-3}eV^2 \quad (2.41)$$

During the stay of the ICARUS experiment at Laboratori Nazionali del Gran Sasso (LNGS), ICARUS measured events with this type of beam.

Very Long-Baseline experiments (VLB), have a source–detector distance larger than LBL experiments by one or two orders of magnitude:

- Reactor VLB measure the combined neutrino flux of many reactors at a distance of the order of $100km$, with a range of L/E and a sensitivity to Δm^2 given by

$$\frac{L}{E} \leq \frac{10^5 m}{MeV} \Rightarrow \Delta m^2 \geq 10^{-5} eV^2 \quad (2.42)$$

KamLAND was an experiment of this type [24].

- Accelerator VLB is accelerator neutrino experiments with a source-detector distance of the order of several thousands of km, comparable with the diameter of the Earth. They cover the range of L/E and the sensitivity to Δm^2 given by

$$\frac{L}{E} \leq \frac{10^4 km}{GeV} \Rightarrow \Delta m^2 \geq 10^{-4} eV^2 \quad (2.43)$$

ATMospheric neutrino experiments (ATM). Cosmic rays that interact with the atmosphere produce a large flux of pions and kaons that decay into muons and neutrinos. The muons later decay into electrons and neutrinos before hitting the ground. The neutrinos that can be detected cover a range of energies from 500 MeV to 100 GeV. The distance between the detector and the source is 20 km at 1.3×10^4 km. Therefore in ATM the range of L/E and the sensitivity to Δm^2 given by

$$\frac{L}{E} \leq \frac{10^4 km}{GeV} \Rightarrow \Delta m^2 \geq 10^{-4} eV^2 \quad (2.44)$$

SOLar neutrino experiments (SOL).

These experiments detect the neutrinos coming from the Sun. Considering the distance between the Sun and the Earth of about 1.5×10^{11} m, and the detectable energy of the solar neutrinos in the range of 0.2-15 MeV, the range of L/E and the sensitivity to Δm^2 are

$$\frac{L}{E} \leq \frac{10^{12} m}{MeV} \Rightarrow \Delta m^2 \geq 10^{-12} eV^2 \quad (2.45)$$

The Table 2.1 shows a summary of the types of neutrino experiments.

	Type of experiment	L/E	Δm^2
SBL	Reactor	$\leq 10 \text{ m/MeV}$	$\Delta m^2 \geq 0.1 \text{ eV}^2$
	Accelerator Pion DIF	$\leq 1 \text{ km/GeV}$	$\Delta m^2 \geq 1 \text{ eV}^2$
	Accelerator Muon DAR	$\leq 1 \text{ m/MeV}$	$\Delta m^2 \geq 1 \text{ eV}^2$
	Accelerator Beam Dump	$\leq 10^{-2} \text{ m/MeV}$	$\Delta m^2 \geq 10^2 \text{ eV}^2$
LBL	Reactor	$\leq 10^3 \text{ m/MeV}$	$\Delta m^2 \geq 10^{-3} \text{ eV}^2$
	Accelerator	$\leq 10^3 \text{ m/GeV}$	$\Delta m^2 \geq 10^{-3} \text{ eV}^2$
VLB	Reactor	$\leq 10^5 \text{ m/MeV}$	$\Delta m^2 \geq 10^{-5} \text{ eV}^2$
	Accelerator	$\leq 10^4 \text{ km/GeV}$	$\Delta m^2 \geq 10^{-4} \text{ eV}^2$
	ATM	$\leq 10^4 \text{ km/GeV}$	$\Delta m^2 \geq 10^{-4} \text{ eV}^2$
	SOL	$\leq 10^{12} \text{ m/MeV}$	$\Delta m^2 \geq 10^{-12} \text{ eV}^2$

Table 2.1: Types of neutrino oscillation experiments.

2.3 The Experimental Anomalies

As mentioned, neutrinos interact through weak and gravitational interactions. However, the hypothetical neutrino introduced by Bruno Pontecorvo in 1967 named sterile neutrino interacts only through gravitational force, and its existence must be indirectly observed through the mixture of neutrinos of the standard model by adding a sterile neutrino, the $3 + 1$ scenario, which leads to new oscillation effects. Neutrino oscillations are characterized by mass splittings: solar $\Delta m_{\odot}^2 \approx 7.4 - 5 \times 10^{-5} \text{ eV}^2$, atmospheric $|\Delta m_{atm}^2| \approx 2.5 \times 10^{-3} \text{ eV}^2$, and mixing angles $\nu_{12} = 34^\circ$, $\nu_{13} = 8.6^\circ$ and $\nu_{23} \approx 45^\circ$ [25]. Experiments have reported anomalies that have been interpreted as an indication of this oscillation, which has led to the development of a new generation of precision experiments.

Indications of the existence of the sterile neutrino are the anomalies observed in the short-baseline experiments. The Liquid Scintillator Neutrino Detector (LSND) at the Los Alamos National Laboratory is optimized to observe electron neutrino events via inverse beta decay process in carbon, $\bar{\nu}_e p \rightarrow e^+ n$, using Cherenkov and scintillation light. LSND consists of a pion DIF source that produces a flux of $\bar{\nu}_\mu$, with energies of up to 53 MeV, the scintillation liquid detector is located approximately 30 m from the source. The main backgrounds at LSND were $\bar{\nu}_e$ production in the beam stop and π^- decay in flight followed by $\bar{\nu}_\mu p \rightarrow \mu^+ n$ where the μ^+ is misidentified as an e^+ . LSND has observed an excess of $87.9 \pm 22.4 \pm 6.0$ $\bar{\nu}_e$ events over these backgrounds, a 3.8σ deviation from expectations [26]. In the neutrino oscillation formalism, these results lead to an additional mass-squared splitting $\Delta m^2 \geq O(0.1 \text{ eV}^2)$, thus requiring physics beyond the Standard Model. This is the origin of the short-baseline neutrino anomaly [27].

Experiment	Type	Channel	Significance
LSND anomaly	DAR accelerator	$\bar{\nu}_\mu \Rightarrow \bar{\nu}_e$	3.8σ
MiniBooNE anomaly	SBL accelerator	$\nu_\mu \Rightarrow \nu_e$	4.5σ
GALLEx/SAGE	Source-e	$\bar{\nu}_\mu \Rightarrow \bar{\nu}_e$	2.8σ
Reactors anomaly	β -decay	ν_e -disappearance	2.8σ

Table 2.2: Short Baseline Neutrino Anomalies.

MiniBooNE was proposed to test the sterile neutrino hypothesis, just as LSND led to a short-baseline anomaly. MiniBooNE is located on the Booster Neutrino Beam of Fermilab, which can generate neutrino beams of ν_μ or $\bar{\nu}_\mu$. The detector observes Cherenkov light emitted by electrons and muons, the detector is located 540 m from the neutrino production target. The background of MiniBooNE is very different from that of LSND, due to a different configuration in energy and the event signature. Nevertheless, having MiniBooNE higher energy and longer baseline make it sensitive to the same range of L/E , ensuring that MiniBooNE probes a mass squared splitting of $O(1 \text{ eV}^2)$, similarly to LSND [27]. MiniBooNE has observed an excess of electron events in both modes neutrino antineutrino, leading to a 4.7σ deviation from the expected background [28, 29]. Interpreting these results as neutrino oscillations, the MiniBooNE and LSND results are compatible with the short-baseline anomaly.

The disappearance of ν_e and $\bar{\nu}_e$ has also been reported in the detection of neutrinos from nuclear power reactors and in calibration runs of solar neutrino experiments using radioactive sources, being another short-baseline neutrino anomaly. The improvement of uncertainties together with a reassessment of the neutrino flux in reactors led to a change in the ratio of the total observed events over the predicted number of events in various reactor experiments, originating the so-called "reactor anomaly" [27]. On the other hand, in calibration of solar gallium neutrino detectors using intense radioactive neutrino sources [30], the theoretical cross-section for neutrino capture $\nu_e + {}^{71}\text{Ga} \rightarrow {}^{71}\text{Ge} + e^+$ leads to a deficit of 3σ compared to the expected one number of events [31], known as the gallium anomaly.

Chapter 3

ICARUS in Short Baseline Neutrino Program Fermilab.

ICARUS (Imaging Cosmic And Rare Underground Signals) is a physics experiment aimed at studying neutrinos. The Nobel laureate Carlo Rubbia proposed this type of neutrino detector called Liquid Argon Time Projection Chambers (LAr-TPC) in 1977 [32]. ICARUS was inaugurated in 2010 at the Gran Sasso National Laboratory of the INFN (National Institute for Nuclear Physics) in Italy, where it operated until 2014. After having been in Gran Sasso, it was part of CERN (European Organization for Nuclear Research) for two years, finally it was transported to the Fermi National Accelerator Laboratory or Fermilab in 2017, where it forms the far detector for the Short-Baseline Neutrino (SBN) program.

3.1 Short Baseline Neutrino Program.

The SBN program consists of three LAr-TPC detectors aligned with the Booster Neutrino Beam (BNB) at the Fermilab. Figure 3.1 depicts the SBN program where the three LAr-TPC detectors are located Short-Baseline Near Detector (SBND), Micro Booster Neutrino Experiment (MicroBooNE) and ICARUS. Its main goals include searching for new physics and recording millions of neutrino charged-current and neutral-current interactions on argon, particularly eV-scale sterile neutrinos research and neutrino-nucleus scattering at GeV energy scale [33].

The development of the SBN program is motivated to prove the existence of 1 eV mass-scale sterile neutrinos [33]. Sterile neutrinos are not directly observable since they do not interact with the ordinary matter through the weak interaction. Nev-

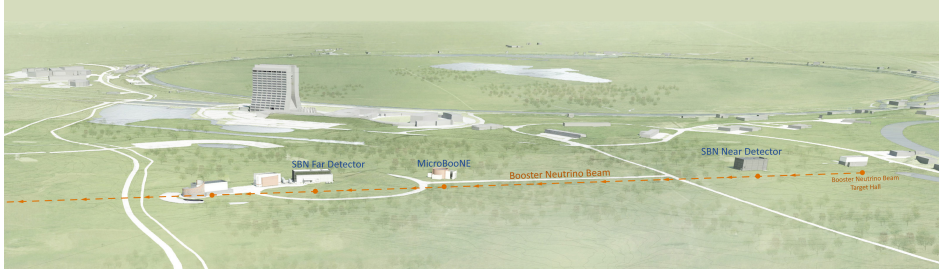


Figure 3.1: View of the Short-Baseline Neutrino experimental area at Fermilab. (<https://sbn.fnal.gov/>)

ertheless active-sterile mixing could generate new oscillations among the standard neutrino flavors. A set of anomalous results in previous neutrino data have been observed in neutrino experiments at a short baseline in the last 20 years (the most significant results are from LSND [34] and MiniBooNE [35, 36, 37]), these anomalies provide hints to indicate there is a fourth and non-weakly interacting sterile type of neutrino.

3.2 Micro Booster Neutrino Experiment.

MicroBooNE is an 80-ton active mass LAr-TPC located 470 m along the BNB. It consists of an 8250-wire TPC and 32 photomultipliers (Figure 3.2). Its principal goal is to address SBN $\nu_\mu \rightarrow \nu_e$ oscillations, primarily observing an excess of electron-like events at low energy that could give hints of physics beyond the Standard Model [35], such as sterile neutrino interactions. MicroBooNE is exposed to the 0.5-2 GeV on-axis BNB and has been collecting data since October 2015. It also is exposed to an off-axis component of the NuMI beam (at 600 m) produced from pion and kaon decays with average neutrino energies of about 0.25 GeV and 2 GeV, respectively. The physics program of MicroBooNE utilizes both BNB and NuMI samples. In addition to oscillation analyses, MicroBooNE performs a suite of precision cross-section measurements, critical for future LAr-TPC detectors, oscillation experiments, and for understanding neutrino interactions in general. Its program also encompasses searches for supernova and proton decay, can record neutrinos from a galactic supernova resulting in current neutrino interactions in the detector's active volume [38].

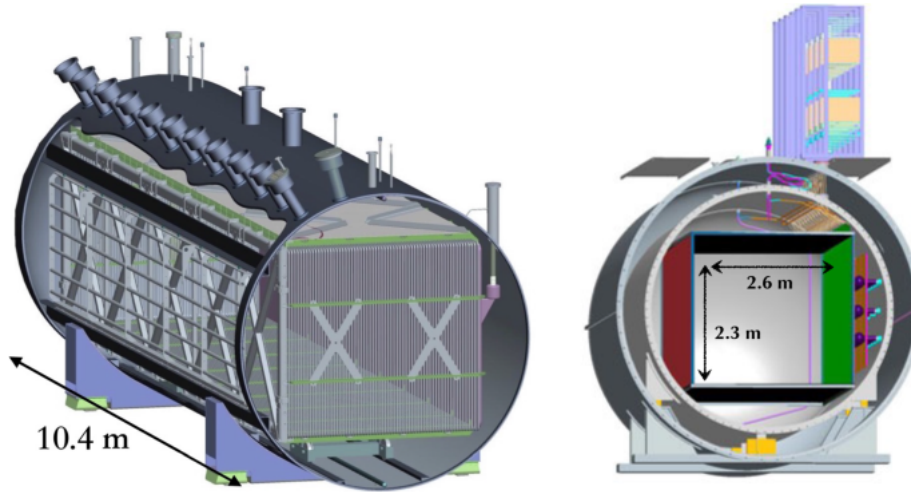


Figure 3.2: A schematic view of the MicroBooNE detector. In the right-hand image are shown the three wire planes of the TPC, the PMTs (not shown) are located behind the wires. Image from [3].

3.3 Short Baseline Near Detector.

SBND is a 112-ton LAr-TPC neutrino detector located 110 m from the target of BNB [39]. It operates inside a membrane cryostat similar to ProtoDUNE and Deep Underground Neutrino Experiment (DUNE) technology [40]. SBND has the main role of measuring the neutrino flux before oscillations occur. Due to its proximity to BNB, SBND is exposed to a high neutrino flux, giving a huge amount of neutrino-argon interaction data, resulting in a rich cross-section program [41]. SBND measures the un-oscillated beam flavor composition to enable precision searches for neutrino oscillations via neutrino appearance and muon neutrino disappearance in the far detectors. Also, it performs detailed studies of the physics of neutrino-argon interactions even in rare channels due to a data sample of millions of neutrino interactions [41].

3.4 Booster Neutrino Beam (BNB) and Neutrin- os at the Main Injector (NuMI).

Booster Neutrino Beam (BNB) is a source of neutrinos generated by the accelerator Booster at Fermilab, Figure (3.4). The proton beams enter the Fermilab Booster synchrotron from the linear accelerator (Linac), accelerating through its 474.20 m

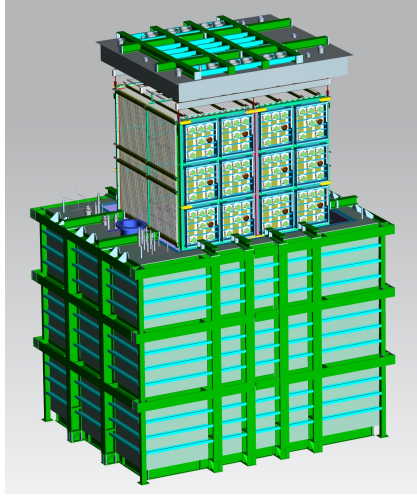


Figure 3.3: The Short-Baseline Near Detector (SBND). Image from <https://sbn-nd.fnal.gov/>.

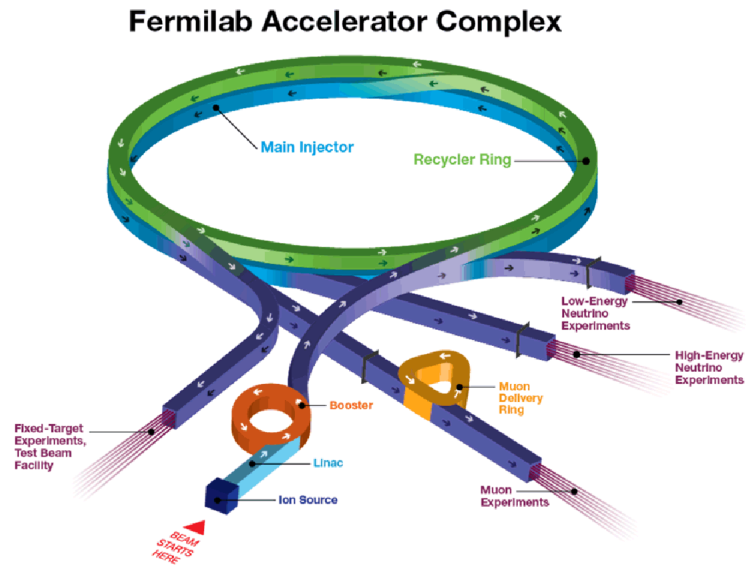


Figure 3.4: Four particle accelerators and storage rings comprises the Fermilab accelerator complex. Image from <https://www.fnal.gov/pub/science/particle-accelerators/accelerator-complex.html>.

Particle	Lifetime [ns]	Decay mode	Branching ratio [%]
π^+	26.03	$\mu^+ + \nu_\mu$	99.9877
		$e^+ + \nu_e$	0.0123
K^+	12.385	$\mu^+ + \nu_\mu$	63.44
		$\pi^0 + e^+ + \nu_e$	4.98
		$\pi^0 + \mu^+ + \nu_\mu$	3.32
K_L^0	51.6	$\pi^- + e^+ + \nu_e$	20.333
		$\pi^+ + e^- + \bar{\nu}_e$	20.197
		$\pi^- + \mu^+ + \nu_\mu$	13.551
		$\pi^+ + \mu^- + \bar{\nu}_\mu$	13.469
μ^+	2197.03	$e^+ + \mu_e + \bar{\nu}_\mu$	13.469

Table 3.1: BNB neutrino production. The corresponding decays of the negative particles are the charge conjugates listed here [2].

ring until reaching an energy of 8 GeV, subsequently, the proton beam is steered at a beryllium target [42]. Mainly pions π and a significant amount of kaons K mesons are produced by the interaction of protons with the beryllium target, which decays producing a neutrino beam with an average energy of 800 MeV [43].

The BNB beryllium target is incorporated into a pulsed electromagnet (horn) that produces a toroidal magnetic field. The polarization of the horn focuses positive or negative mesons, allowing to produce a beam of neutrinos ν 's or antineutrinos $\bar{\nu}$'s. Table 3.1 lists the particles produced by BNB [43]. The decay of pions π 's produces muons which also leads to the production of neutrinos, which results in a more significant flux in $\nu_e/\bar{\nu}_e$ than that of $\nu_\mu/\bar{\nu}_\mu$.

The Neutrinos at the Main Injector (NuMI) neutrino beam was built at Fermilab to provide neutrinos for different neutrino oscillation experiments. NuMI directs a beam of 120 GeV protons from Fermilab's Main Injector onto a graphite target, it is one of the most powerful neutrino beams in the world. Similar to BNB, NuMI creates a neutrino beam from the decays of pions and kaons [44]. The NUMI proton beam is located at ~ 700 m from ICARUS and at an off-axis angle of 6 degrees.

Section 4.3 talks about the selection of ICARUS events, in which I participate. During the learning of the ICARUS tools most of the observed events were from the BNB beam and a few from the NuMI beam.

Chapter 4

Design of ICARUS detector.

4.1 A new concept for neutrino detectors.

Carlo Rubbia proposed in 1977 a new type of neutrino detector in his work titled *The Liquid Argon Time Projection Chamber: A New Concept for Neutrino Detectors* [32]. Before this proposal, neutrino experiments were divided into two classes, high-resolution bubble chambers with a relatively small sensitive mass and electron detectors in which only a few of the features of events are observed in a much more massive target volume. Scientists needed a new device that would combine or raise the characteristics of these types of experiments.

Charpak, in 1970 [45], introduced the concept of Time Projection Chamber (TPC), the idea consists of drifting the electron image of an event occurring in a noble gas towards a collecting multielectrode array which is capable of reconstructing the three-dimensional image of the event from the 2D information of the read-out wire plane and the drift time t .

Instead of using a gas as the active volume, the use of LAr was proposed. The LAr has adequate properties to work together with TPCs, since it is dense (1.4 g/cm^3), it is cheap, it is inert, it is easy to obtain and purify, and the most important, it does not attach electrons and hence it permits long drift-times and a high electron mobility inner the LAr [32].

By combining the design of the TPCs and the LAr, a new type of neutrino detector is born, the LAr-TPCs. It was conceived as a tool for a completely uniform imaging with high accuracy of massive volumes. The operational principle of the LAr-TPCs is based on the fact that in highly purified LAr ionization tracks can be transported practically undistorted by a uniform electric field over macroscopic

distances [32]. Imaging is provided by a suitable set of electrodes (called TPC wires or wire planes) placed at the end of the drift path continuously sensing and recording the signals induced by the drifting electrons [46]. With this device it is possible to detect the signal of the electrons that pass through the different wire planes with different orientation, since it is possible to carry out a non-destructive reading of the electrons by induction of charge. In this way it is possible to obtain different projections of the same event, which will allow the reconstruction of spatial points and a precise calorimetric measurement.

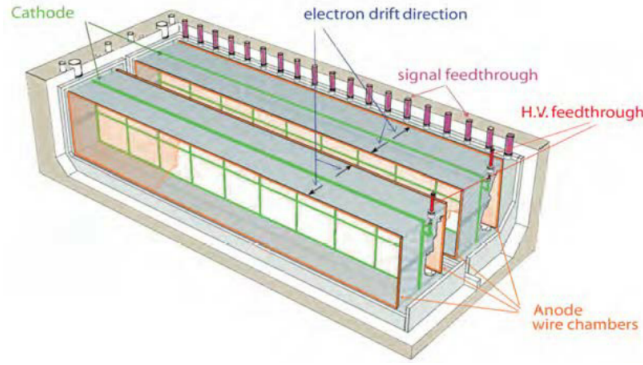


Figure 4.1: ICARUS T600 detector schematics, showing both modules and the common insulation surrounding the detector; inner structures and feed-through's are also shown. On the bottom a view of the detectors is presented with the wire chambers and the high voltage system (race-tracks and cathodes). Image from [4]

4.2 ICARUS T600 Detector Overview.

ICARUS T600 is composed of two identical cryostats with dimensions of 3.6 m (width) x 3.9 m (height) x 19.6 m (length), placed side by side, each one surrounded externally by layers of thermal insulation. Each of these modules was called "T 300". Inside each T300 there are two TPCs, each one with three wire planes separated by 3 mm and oriented at 60° with respect to each other, the total number of wires used in the T600 is 53 248 [46].

The electric field that guides the drift of the ionization electrons is perpendicular to the wire planes and is established in the LAr volume of each T300 using a High Voltage (HV) system. The system is composed of a cathode located in the center of each T300 module between each pair of TPCs at 1.5 m, which is the maximum drift path (during the development of ICARUS, it was concluded that the LAr-TPCs technology would allow for drift distances exceeding 3 m [47]). To guarantee the uniformity of the electric field along the drift direction field, field-shaping electrodes are used, while the HV system supplies the required voltage at the cathode. The cathode is supplied with a nominal voltage of 75 kV, which results in an electric field of 500 V/cm [46].

The read-out electronics are located outside the detector. On the top side of the cryostats are housed the exit flanges equipped with cryogenic feedthroughs for the electrical connection of the wires with the read-out electronics, and for all the internal instrumentation (PMTs, LAr purity monitors, level and temperature probes, etc.) [46].

4.3 Description and operation of LAr-TPCs in ICARUS detector.

The chambers are composed of a TPC, a cathode, and the LAr between them. Inside each T300, there are two chambers (called left and right chambers) with a common cathode. The separation between the TPCs in each T300 is 3 m. The cathode placed in the middle of the TPCs is a parallel plane to the wires planes. Each chamber has a volume of 1.5 m (the drift length) x 17.95 x 3.16 m² (surface of the wire planes) [46].

ICARUS TPCs have three wire planes. Each of the planes of the TPC provides a two-dimensional projection of the event image, with one coordinate given by the wire position and the other given by the drift distance. The different projections on the three wires planes have as a common coordinate the drift distance, then a full 3D reconstruction of the event is obtained by correlating the signals from two different planes at the same drift distance.

The directions of the three wire planes are 0°, +60°, and -60° with respect to the horizontal direction (Figure 4.2). The separation between each plane is 3mm. The first plane (0°) and second plane (+60) facing the drift volume work in induction mode and are called Induction-1 plane and Induction-2 plane, while the third plane (-60°) works in charge collection mode called Collection plane (in both right and left chamber). To ensure that the electron image reaches the charge collection plane after having passed through the first two induction planes, a nondestructive read-out is performed by polarizing all planes to suitable potentials. These potentials are given by the following relationship between the electric fields in the LArTPC active volume and the wires planes: $E_2 \leq F \times E_1$, $E_1 \leq F \times E$, where E_1 is the field value in the induction-1 to Induction-2 gap, and E_2 the field value in the Induction-2 to Collection gap, $E = 500V/cm$ is the nominal value of the electric field in the LArTPC active volume, and F is a field scaling factor which takes the values of 1.2 to 1.5 [46].

In Standard Model theory, neutrinos interact through weak charged current or neutral current with the argon atoms. The resulting charged particles ionize and excite the argon atoms in the detector volume as they propagate emitting scintillating light (see Figure 4.3) [5]. The ionization process allow detecting neutrinos in the LAr-TPCs since the produced free electrons will be guided to the TPCs due to the presence of the electric field. As a result, a collection of waveforms is obtained whose amplitude depends on the number of electrons collected. The waveforms will change as the particles are more or less ionizing than others. By studying the waveforms, it is possible to obtain a preview of the event that will later go from a collection of

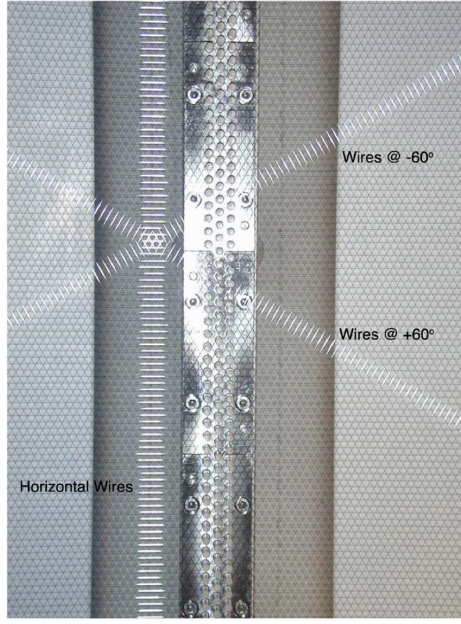


Figure 4.2: The three wire planes of a TPC installed in the T600 detector.

signals to 2D images for each LArTPC. Figure 4.4 shows the operational principle of the TPCs.

The LAr TPC is a medium in which Cherenkov radiation can be detected. This radiation is produced by the passage of electrically charged particles in a given medium at speeds greater than the speed of light. The wavelength of the scintillation light emitted by LAr is approximately 128 nm, which is in the vacuum ultraviolet (VUV) spectral region.

The use of LAr in ICARUS is motivated by the reasons given by Carlo Rubia in the original conceptual design of the LArTPC type detectors. Ionization and scintillation are processes that characterize LAr. The average energy to produce an electron-ion pair is $W_{ion} = 23.6\text{eV}$, while for a scintillation photon emission is $W_{ph} = 19.5\text{eV}$ [46]. Both processes are complementary and depend on the field applied to the active LAr volume. In the case of ionization, the number of free electrons rises with the value of the electric field, while the photons in the scintillation process decrease. However, for fields higher than 10kV/cm both cases are saturated, and at the value of the electric field in ICARUS of 500V/cm both processes are active.

The complexity and quantity of data collected by high energy physics experiments makes it difficult to visualize such data. Visualizing neutrino events in LArTPC-type experiments is of fundamental importance to understand their properties, in addition to being also important for the monitoring and correct operation

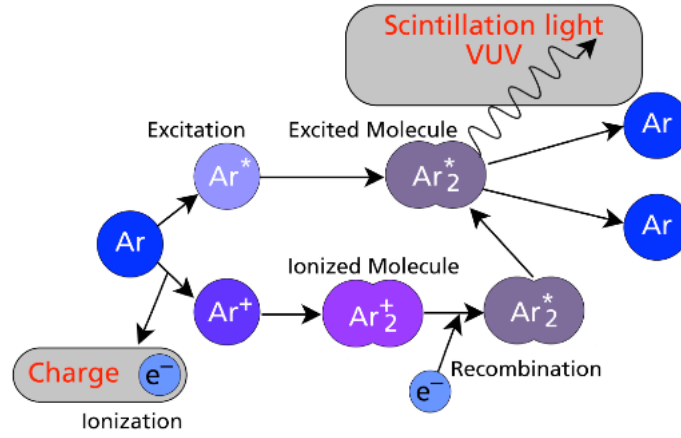


Figure 4.3: Scintillation and ionization mechanism of liquid argon. Image from [5]

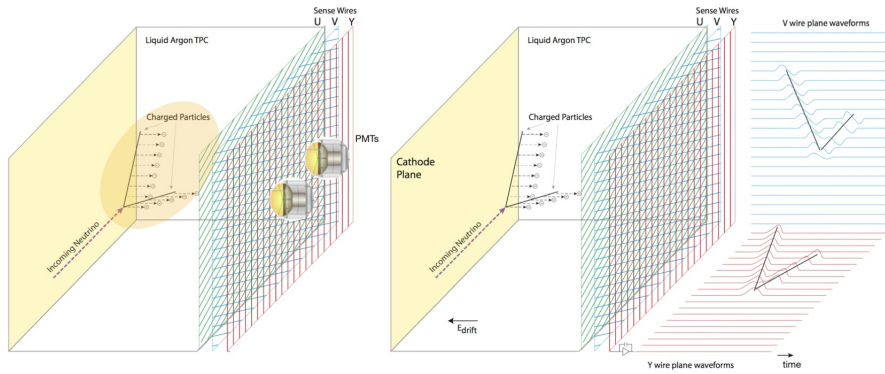


Figure 4.4: The electric field generated between the cathode and the anode (wire planes) acts on the electrons, leading them to the wire planes, where a signal is obtained when interacting with each wire plane, which will later be used in the reconstruction of the event. Image from [6].

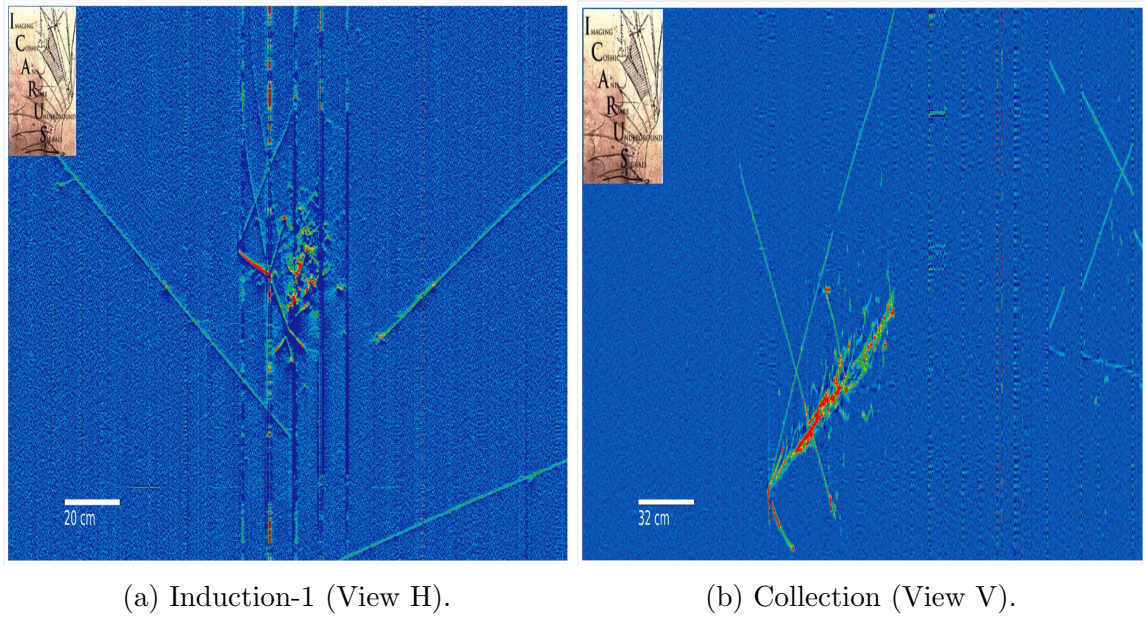


Figure 4.5: Event 1166, ν_μ -candidate.

of the detector. The LArTPC experiments provide incredible insights into neutrinos, which is why a visualization tool is necessary. TITUS is a piece of software developed for this purpose. The event monitor to visualize the interactions in the Fermilab TPCs is TITUS.

In the developing this thesis, it was essential to understand and use different tools developed within Fermilab, and this event monitor is one of them. To understand how the LArTPC works and how to find the interactions with this device, I visualized a large number of real events obtained by ICARUS as part of the scanning effort carried out since January of this year. The objective of the scanning effort is to visualize one by one real events collected by ICARUS.

The members of the CINVESTAV-ICARUS collaboration did the scanning to classify and report the possible candidates found by the detector, while a group of experts verifies the information obtained with LArSoft algorithms that implement automatic event identification. Examples of candidate events confirmed as neutrino interactions are shown in Figure 4.5a and 4.5b. We can see the reconstruction of a ν_μ candidate by the Induction-1 and Collection wire planes. Figure 4.6 shows the Induction-2 reconstruction. These examples are events found in the data assigned to me by the collaboration during the scanning effort.

Monte carlo simulation estimates that 28,000 events are found in ICARUS per day, per pulse and repetition rate of the BNB (5 Hz) and NuMi (0.75 Hz) beams.

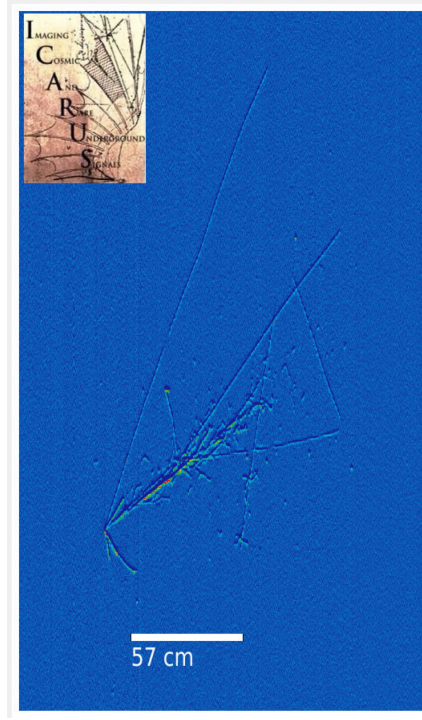


Figure 4.6: Event 1166, ν_μ -candidate. Induction-2 (View U).

Table 4.1 shows the type of events expected per day in both beams. In each collection of events, more than 10 cosmic muons are expected that are randomly overlapped in the signal wire for 1 ms.

The main goal of event selection is to identify neutrino interactions, eliminating background interactions, mainly cosmic rays. The combination of the different signals obtained by the TPCs, the PMTs and the Cosmic Ray Tracker (CRT) system and the reconstruction tools developed in ICARUS and SBN is crucial to reject the background.

The identification of muon neutrinos ν_μ in CC interactions is characterized by a track longer than 50 cm if it stops inside the detector or longer than 1 m if it is not fully contained. Electromagnetic showers connected with the primary vertex are observed in the case of electron neutrino ν_e events.

The MC simulations and the the scanning efforts have confirmed 81 ν_μ CC recognized events from BNB beam, 230 recognized ν_μ CC candidate events from NuMI beam and 18 ν_e CC candidate events from NuMI beam to be studied. Table 4.2 shows a summary of the status of the event selection.

Beam	Neutrino events/day	Type of event
BNB	8000	cosmics
	2500	ν interaction (1900 ν_μ CC)
	2200	beam halo interactions
NuMI	6500	cosmics
	4300	ν interaction (2500 ν_μ CC)
	4300	beam halo interactions

Table 4.1: MC calculations of expected event rates in ICARUS-T600.

RUN	CRYO	BEAM	PURITY	ν_μ CC	ν_e CC	Event Studied	P.O.T. 10^{17}
5252	WEST	BNB	2.7 ms	19	0	600	1
5507	WEST	NuMI	2.8 ms	24	2	716	1.7
	EAST		3.2 ms				
5510	WEST	NuMI	2.8 ms	77	1 (+2 to be studied)	943	2.25
	EAST		3.2 ms				
5679	WEST	NuMI	2.7 ms	46	2(+4 to be studied)	863	2
	EAST		3.1 ms				
5795	WEST	BNB	2.1 ms	15	0	790	0.6
	EAST		3.2 ms				
5873	EAST	BNB	3.3 ms	85	4(+4 to be studied)	1800	BNB: 2.8 NuMI: 6.2
		NuMI					
6030	EAST	BNB	3.0 ms	33	(1 to be studied)	1310	BNB: 0.36 NuMI: 0.75
	WEST	NuMI	4.2 ms				
6105	EAST	only BNB studied	3.2 ms	12	0	786	0.5
	WEST		4.5 ms				

Table 4.2: Summary of Scanning Efforts ICARUS 2021. In all runs the trigger was MinBias except for run 6105 where it was Majority 5.

4.4 The internal PMT system

To detect scintillation light in LAr, we need a system of Photomultipliers (PMTs). PMTs are a type of optical vacuum detector that takes advantage of the effect of secondary emission of electrons to respond to very low illumination levels, maintaining an acceptable noise level, they are mainly used in particle experiments based on Cherenkov radiation. Scintillation in LAr is characterized by a prompt $< 2\mu s$ photon emission in the VUV spectrum with $\lambda = 128nm$ and by a yield of the order of $10^4/MeV$, hence providing an absolute time measurement and a trigger for ionizing events occurring in LAr [46].

The PMTs adopted in ICARUS are the 9357FLA Electron Tubes PMTs: 12-stage dynode PMTs with hemispherical 200 mm (8 in) diameter glass windows, manufactured to work at cryogenics temperatures [46]. Figure 4.7 illustrate the design of the device.

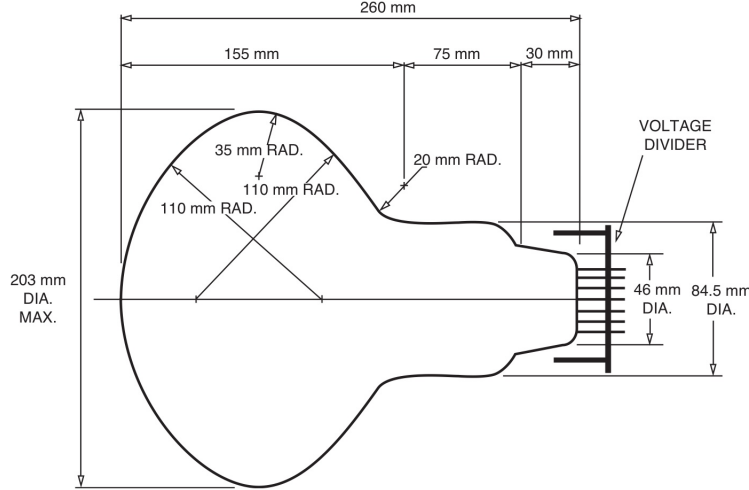


Figure 4.7: Scheme of 9357 FLA Electron Tubes PMTs.

ICARUS carried out careful evaluation of the performance of each PMT before the final mounting in the detector. The measurements focused on the main PMT parameters, which are temperature dependent, to select the best PMT sample to use in the T600. In particular, ICARUS investigated the following features for each PMT:

- Shape of the anode pulse.
- Single-electron response of the anode pulse.

- Gain.
- Single-electron transit time (spread, pre- and late-pulsing).
- After-pulses.
- Dark-count rate and spectrum.

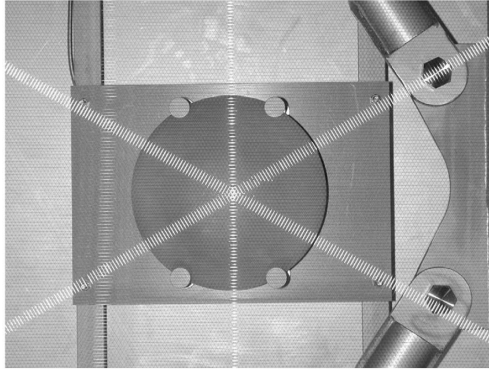


Figure 4.8: PMT visible behind the three wire planes.

The PMT glass window is not transparent to the 128 nm scintillation light. Therefore, it was necessary to coat the device with a proper fluorescent wavelength shifter to be sensitive to the LAr VUV photons. The PMTs are placed behind the wire plans (Figure 4.8). 90 PMTs are placed in each TPC plane, giving a total of 360 PMTs. Figure 4.9 shows a TPC, and the PMTs placed there [46].



Figure 4.9: PMTs placed in one of the ICARUS TPCs. Image from: <https://icarus.fnal.gov/>.

Chapter 5

Muon Tracking

The trace of the muons in the ICARUS detector is important in the background identification process. The measurement of the times of the photons or electrons in the scintillation and ionization processes is vital for identifying and selecting events of interest to researchers.

The goal is to reconstruct the muon trajectory using the information from the PMTs. To reconstruct the muon track, the following steps must be carried out: (1) Prediction of the arrival time for the first photon emitted by the muon in the PMTs. (2) Compare the predicted First Hit Time (FHT) with that observed in a Monte Carlo simulation for a single muon. (3) Obtain the muon reconstruction parameters.

5.1 Optical Model

We begin by developing the model that predicts the time of the first photon that reaches the PMTs.

When a muon travels in ICARUS cryostats through LAr, the energy deposited in LAr emits scintillating light isotropically along the muon track. Cherenkov radiation is almost completely absorbed by LAr and re-emitted as scintillating light [5, 48]. For this reason, very few photons produced by the Cherenkov effect reach the PMTs that can give us information on the direction of the muon's trajectory. Since it is difficult to distinguish the photons produced by the scintillation and Cherenkov effect, all lights are treated as isotropic in the derivation of the optical model.

The photons emitted by the muon will travel through the LAr, some of them reaching the PMTs. For a specified PMT, we identify the earliest one as the fastest

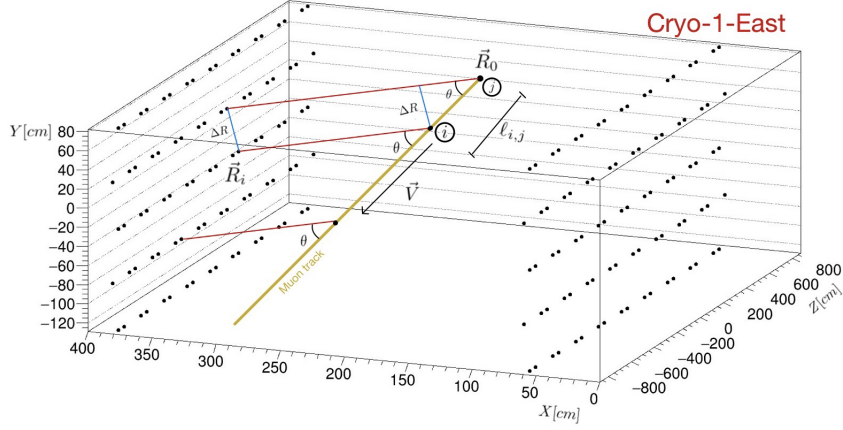


Figure 5.1: Schematic of the optical model that predicts the First Hit Time of the ICARUS PMTs. A muon is shown traveling through cryostat 0 east. \vec{R}_i is the position of the i th PMT, \vec{R}_0 is the injecting position of the muon track into the LAr, \hat{V} is the direction of the muon track, ΔR is the distance between the PMTs that turn on, $\ell_{i,j}$ is the distance between the emission points of the photons, and θ is the Cherenkov angle.

light of this PMT among all the photons hit on it. The fastest light hit on the PMT is defined as the first hit time (FHT). The FHT of a PMT at position \vec{R} is predicted using the tracking parameters with a proper optical model,

$$T_i^{pre} = f(\vec{R}_i, \vec{R}_0, t_{inj}, \hat{V}, \ell_{i,j}), \quad (5.1)$$

and depends on the following parameters: $\vec{R}_i = (x_i, y_i, z_i)$ is the position of the i^{th} PMT, \vec{R}_0 is the initial position of the muon injected into the liquid argon, t_{inj} is the injection time of the muon into the LAr, \hat{V} is the unit vector in the direction of the muon track, and $\ell_{i,j}$ is the distance between the emission points of the photons that are FHT of the PMTs (see Figure 5.1 and 5.2). The straight track of muon in the detector can be described by these parameters.

The optical model predicts the minimal arrival time of the photon to the detector. The arriving time of a photon at a certain PMT can be calculated as:

$$t = t_{inj} + t_{muon} + t_{photon}, \quad (5.2)$$

where t_{muon} is the propagation time of the muon at a distance $\ell_{i,j}$

$$t_{muon} = \frac{\ell_{i,j}}{c_\mu}, \quad i \neq j, \quad (5.3)$$

the subscripts i and j indicate two different PMTs participating in the event. The variable $\ell_{i,j}$ will be derived by the geometry of the Figure 5.2. t_{photon} is the time of

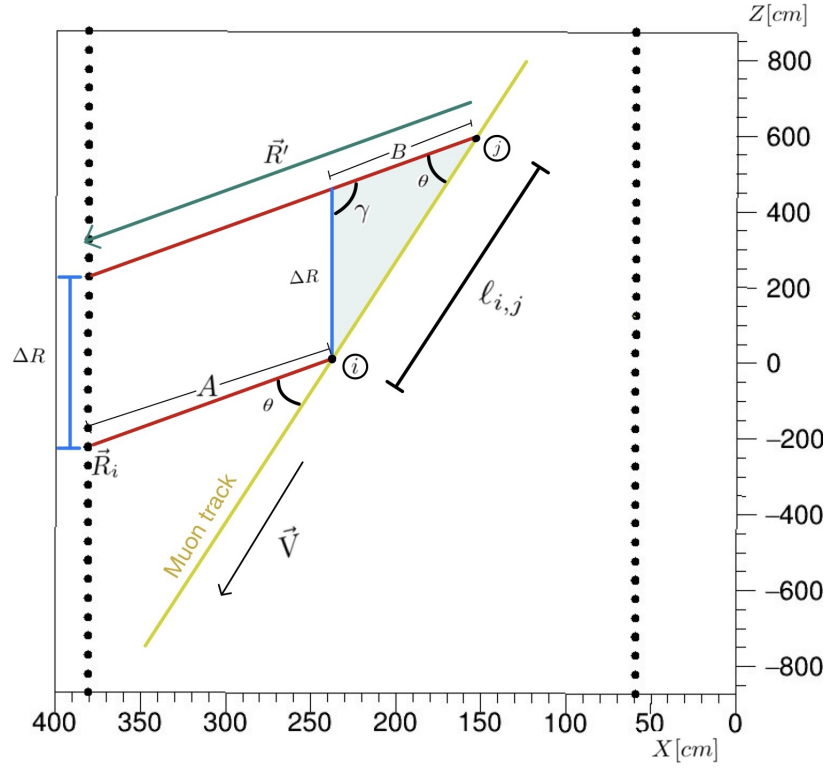


Figure 5.2: Top view of Cryostat-1-East illustrating the geometry used in ICARUS to calculate the variable $\ell_{i,j}$.

flight of this photon

$$t_{\text{photon}} = \frac{|\vec{R}_i - (\vec{R}_0 + \ell_{i,j}\hat{V})|}{c/n_{LAr}}, \quad (5.4)$$

where n_{LAr} is the liquid argon refractive index.

The arrival time of the photon to a certain PMT has the form:

$$t = t_{inj} + \frac{\ell_{i,j}}{c_\mu} + \frac{|\vec{R}_i - (\vec{R}_0 + \ell_{i,j}\hat{V})|}{c/n_{LAr}}. \quad (5.5)$$

To obtain the shortest time in which the photon reaches the PMT \vec{R}_i , we minimize the arrival time with respect to $\ell_{i,j}$, to find a constraint that tells us the first hit time:

$$\frac{\partial t}{\partial \ell_{i,j}} = \frac{1}{c_\mu} + \frac{n_{LAr}}{c} \frac{\partial |\vec{R}'|}{\partial \ell_{i,j}} = 0, \quad (5.6)$$

where \vec{R}' , means the vector going from the emitting point to the PMT \vec{R}_i . To calculate its derivative we define $\vec{R}_{i,0} = \vec{R}_i - \vec{R}_0$. Then

$$\begin{aligned} \frac{\partial |\vec{R}'|}{\partial \ell_{i,j}} &= \frac{\partial (|\vec{R}'|^2)^{\frac{1}{2}}}{\partial \ell_{i,j}} \\ &= \frac{1}{2} (|\vec{R}'|^2)^{-\frac{1}{2}} \cdot \frac{\partial |\vec{R}'|^2}{\partial \ell_{i,j}} \\ &= \frac{1}{2} \frac{1}{|\vec{R}'|} \cdot \frac{\partial \vec{R}'^2}{\partial \ell_{i,j}} \\ &= \frac{1}{2} \frac{1}{|\vec{R}'|} \cdot \frac{\partial (\vec{R}_{i,0}^2 - 2\ell_{i,j}\vec{R}_{i,0} \cdot \hat{V} + \ell_{i,j}^2 \hat{V}^2)}{\partial \ell_{i,j}} \\ &= \frac{1}{2} \frac{1}{|\vec{R}'|} \cdot -2(\vec{R}_{i,0} - \ell_{i,j}\hat{V}) \cdot \hat{V} \\ &= -\frac{\vec{R}'}{|\vec{R}'|} \cdot \hat{V} = \hat{R}' \cdot \hat{V}, \end{aligned}$$

From Figure [5.2](#) we note that the angle between \hat{R}' and \hat{V} is θ , then the derivative of $|\vec{R}'|$ is given by

$$\frac{\partial |\vec{R}'|}{\partial \ell_{i,j}} = -\cos \theta. \quad (5.7)$$

Substituting Eq. [\(5.7\)](#) in Eq. [\(5.6\)](#), we have

$$\frac{\partial t}{\partial \ell_{i,j}} = \frac{1}{c_\mu} - \frac{n_{LAr}}{c} \cos \theta = 0. \quad (5.8)$$

To solve for $\cos \theta$, we consider $c_\mu \approx c$, since muons are relativistic particles, then

$$\cos \theta = \frac{1}{n_{LAr}}. \quad (5.9)$$

This means that the emission angle for the PMTs FHT photons is determined by the angle θ , which is the same as the emission angle of the Cherenkov light.

Using the geometry of Figure 5.2, and the relation in Eq. (5.9), we can calculate $\ell_{i,j}$. First, we take the difference between the arrival time of two photons, (points (i) and (j) in Figure 5.2))

$$T_{(j)} - T_{(i)} = \frac{\ell_{i,j}}{c} + \frac{A}{c/n_{LAr}} - \frac{B+A}{c/n_{LAr}}, \quad (5.10)$$

$$\Delta T = \frac{\ell_{i,j}}{c} - \frac{n_{LAr}B}{c}. \quad (5.11)$$

Solving for B we have

$$B = \frac{c}{n} \left(\frac{\ell_{i,j}}{c} - \Delta T \right). \quad (5.12)$$

Now, using the law of cosines in the triangle of Figure 5.2, we have

$$\Delta R^2 = B^2 + \ell_{i,j}^2 - 2B\ell_{i,j} \cos \theta, \quad (5.13)$$

and substituting B in Eq. (5.13) and solving for $\ell_{i,j}$

$$\Delta R^2 = \frac{1}{n_{LAr}^2} (\ell_{i,j} - \Delta T c)^2 + \ell_{i,j}^2 - \frac{2\ell_{i,j}(\ell_{i,j} - \Delta T c)}{n_{LAr}^2}, \quad (5.14)$$

$$\Delta R^2 = \left(\frac{\Delta T c}{n_{LAr}} \right)^2 - \ell_{i,j}^2 \left(1 - \frac{1}{n_{LAr}^2} \right). \quad (5.15)$$

The variable $\ell_{i,j}$ is vital for the complete reconstruction of the muon trajectory

$$\ell_{i,j} = n_{LAr} \sqrt{\left(\frac{1}{n_{LAr}^2 - 1} \right) (\Delta R^2 - \frac{\Delta T^2 c^2}{n_{LAr}^2})}. \quad (5.16)$$

Also, with the law of sines we can find γ

$$\frac{\sin \gamma}{\ell} = \frac{\sin \theta}{\Delta R}. \quad (5.17)$$

The reconstructed track parameters are obtained by minimizing the χ^2 function

$$\chi^2 = \sum_i \frac{(T_i^{pre} - T_i^{obs})^2}{\sigma_i^2}, \quad (5.18)$$

where T_i^{obs} is the observed value of FHT from data or MC and σ_i represents the error of FHT for the i^{th} PMT.

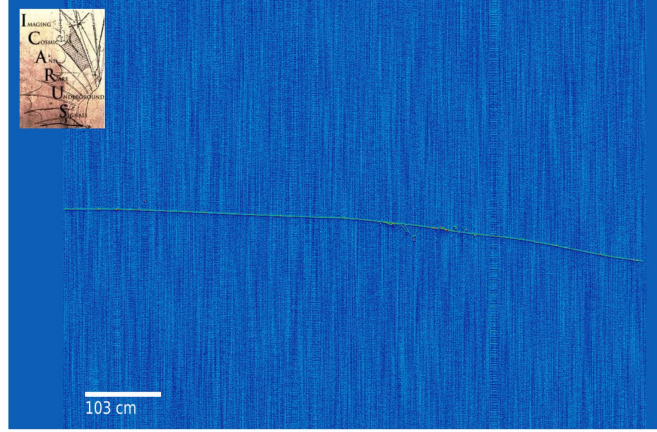


Figure 5.3: Muon simulated using LArSoft, has an energy of 2GeV, and is perpendicular to Induction 1.

5.2 Muon Simulation with LArSoft

LArSoft Collaboration is a group of experiments, laboratories, university groups and software projects, who work together to develop the code that is needed in the LAr-TPCs. LArSoft is a set of detector-independent software tools for the simulation, reconstruction and analysis of data from LAr neutrino experiments. LArSoft is currently used in production, simulation, and reconstruction by the ArgoNeuT, DUNE, LArIAT, MicroBooNE, and SBND experiments. The software suite offers a wide selection of algorithms and utilities, including those for associated photo-detectors and the handling of auxiliary detectors outside the TPCs. Available algorithms cover the full range of simulation and reconstruction, from raw waveforms to high-level reconstructed objects, event topologies, and classification [49].

LArSoft was also a necessary tool to learn for this work. We simulated muons with LArSoft to obtain all the required information for the development of the model. In particular, we will focus here in a muon from BNB beam with an energy of 2 GeV and simulated at 0° with respect to the Z-axis (parallel to Induction 1). See Figure (5.3). The x, y, and z initial coordinates are $(-290.639, -98.1296, -14.1188)$, respectively.

Using LArSoft, we get the information from the ICARUS PMTs. In particular, we are interested in the positions of the PMTs and their FHT that will be implemented in minimizing the χ^2 function to obtain the reconstruction parameters of the optical model.

The positions of the PMTs that turn on during this event are shown in Figure 5.4.

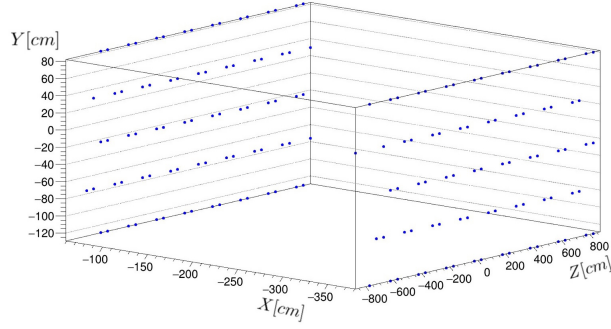


Figure 5.4: PMTs On in the simulated muon.

It is observed that the event takes place in Cryo 0 East and that 157 PMTs, of the 360 available, are lit. A histogram of the FHTs obtained for this event, found with LArSoft, is shown in the Figure 5.5.

This information makes it possible to generate a graph that helps us visualize the information obtained, as shown in Figures 5.6 and 5.7, where a color map represents the intensity of the FHT of each PMT for the event.

LArSoft modules are developed in C^{++} . Therefore, it was natural to write the code that computes the χ^2 in the same language. To develop the code, we generate a series of points that represent the variables to be found. We show, in Figure 5.8, the points that represent the possible values of \vec{R}_0 for the muon. Possible \vec{R}_0 values are within the volume of the detector. To find the time in which the muon enters the scintillating liquid, that is, the variable t_{inj} , we consider as a first approximation that the FHT with the lowest magnitude among all the FHTs captured by the PMTs corresponds to the muon injection time. With this information we can leave this variable as fixed and change the others to find the minimum χ^2 .

The variable $\ell_{i,j}$ is given by the Eq. (5.16). To minimize the χ^2 function, we consider that ΔR (see Figure 5.2), is given by

$$\Delta R_{F,i} = |\vec{R}_F - \vec{R}_i| \quad (5.19)$$

where \vec{R}_F is the position of the PMT that has the first FHT i.e. the FHT with lowest value, and \vec{R}_i are the PMTs turn on during the event detection.

After running the code for this study case, the χ^2 function gave as a minimum the direction of the muon in the Z direction. That is, as expected, the muon direction was found to be $\vec{V} = (0, 0, 1)$. In this sense, the code found a first positive result, which is encouraging.

Besides, also the X and Y coordinates of the injection vector were found. For the

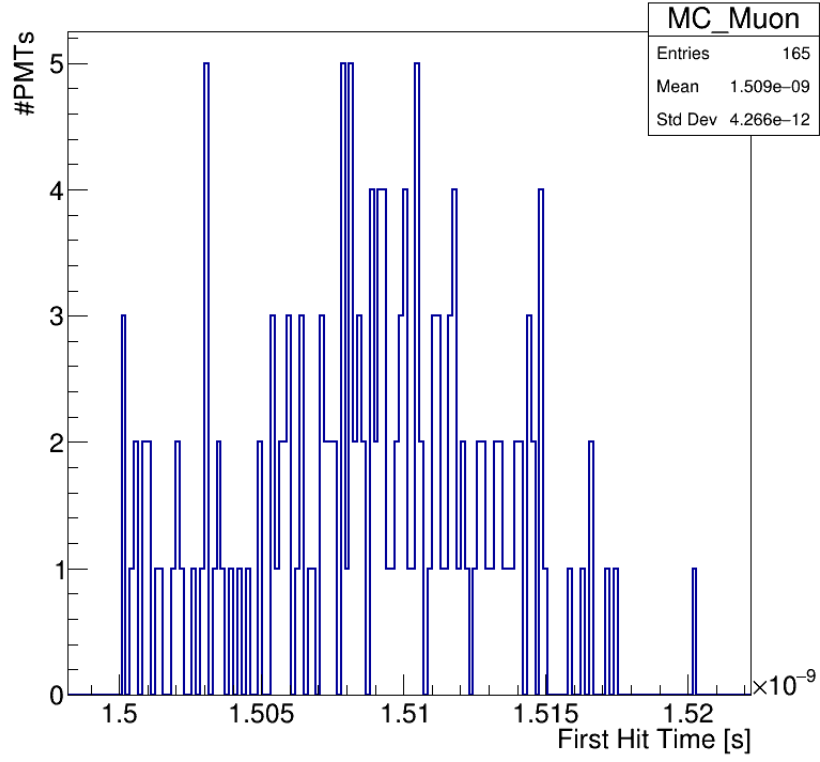


Figure 5.5: Histogram of the Monte Carlo data from the simulated muon FHT.

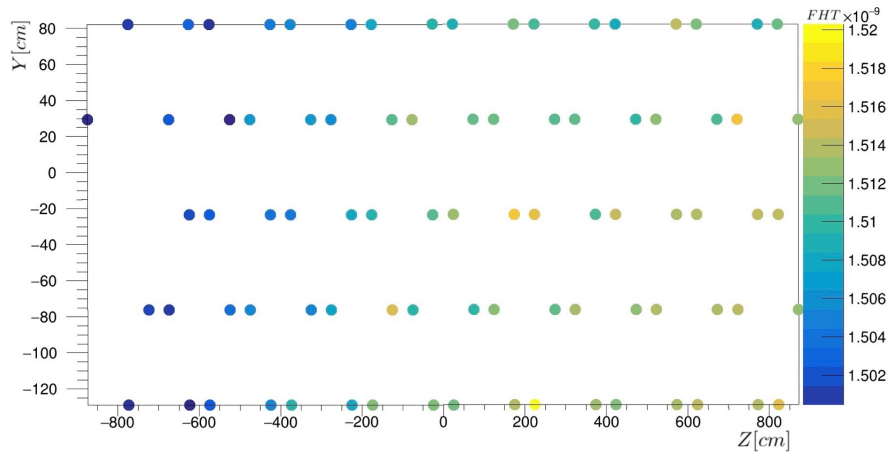


Figure 5.6: FHT in the PMTs on the plane located at $x = -59.36$ cm.

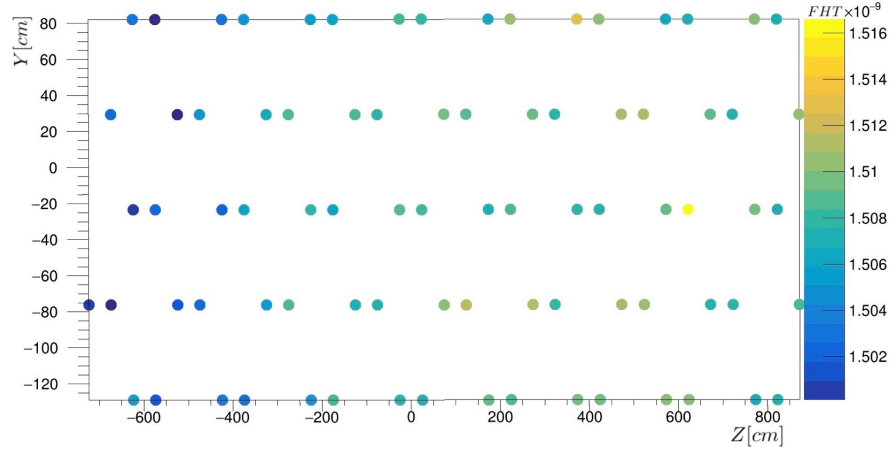


Figure 5.7: FHT in the PMTs on the plane located at $x = -381.07$ cm.

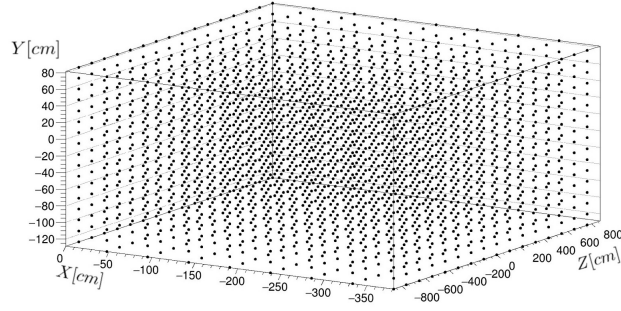


Figure 5.8: Points that represent the position of the possible Ro for the event.

calculation of the Z coordinate of the injection vector, a series of proposals and perspectives have been made as to why there is no resolution in that direction. Figures 5.9, 5.10, and 5.11 show the graphs of the χ^2 vs the injection point components.

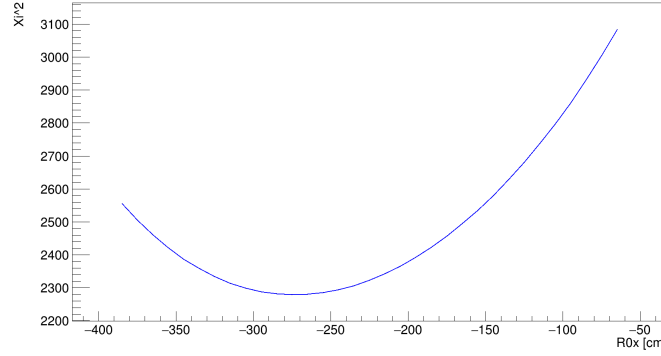


Figure 5.9: χ^2 vs \vec{R}_{0x} . The sample was a muon with an energy of 2GeV with an angle of 0 ° with respect to the Z axis. $\vec{R}_{0x} = -275$ cm is the predicted value.

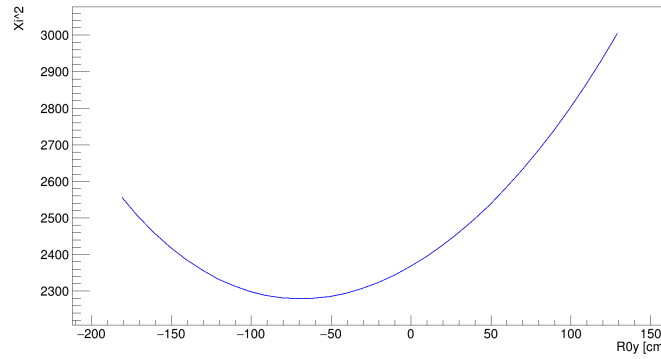


Figure 5.10: χ^2 vs \vec{R}_{0y} . $\vec{R}_{0y} = -71$ cm is the predicted value.

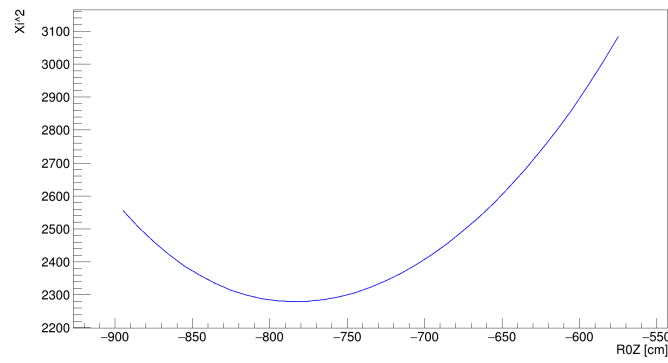


Figure 5.11: χ^2 vs \vec{R}_{0z} . $\vec{R}_{0z} = -785$ cm is the predicted value.

Chapter 6

Conclusion and Perspectives

ICARUS is a new experiment from which great results are expected. The process of improving the reconstruction of events and elimination of the background is currently under construction. Although ICARUS is a LArTPC-type experiment, it is essential to use PMTs to detect scintillating light produced by the different events occurring in the LAr active volume. The light detection system has been improved since its inception in the Gran Sasso Underground Laboratory. In particular, the number of PMTs was increased from 20 to 90 per T300 module [46, 48]. The 3D track reconstruction of the TPC wires is complemented by the scintillating light detection system, contributing to the identification of neutrino interactions from BNB and rejection of the cosmic background.

As far as we know, the model presented in this thesis attempts to reconstruct for the first time the trajectory of the muons in a LArTPC type detector using only information from the scintillation system (positions of the PMTs and FHTs). Comparing this reconstruction with that obtained from the TPC wires may help to improve the classification of events in ICARUS. The FHT approach will be used in the Jiangmen Underground Neutrino Observatory (JUNO) experiment, which is a multipurpose neutrino experiment, whose detection system is completely made up of PMTs [50]. JUNO consists of 20-kton of scintillation liquid and 18,000 PMTs on the surface of a sphere that is the central detector.

In the development of the thesis, the geometry of the ICARUS PMTs was the primary consideration. Despite not being the central system, the PMTs could be able to reconstruct the muon trajectories. Therefore, to improve the results, a series of proposals adapted to the ICARUS features are presented as a perspective for this work that we plan to continue, Which can be extended from the master's thesis but could continue within the ICARUS collaboration.

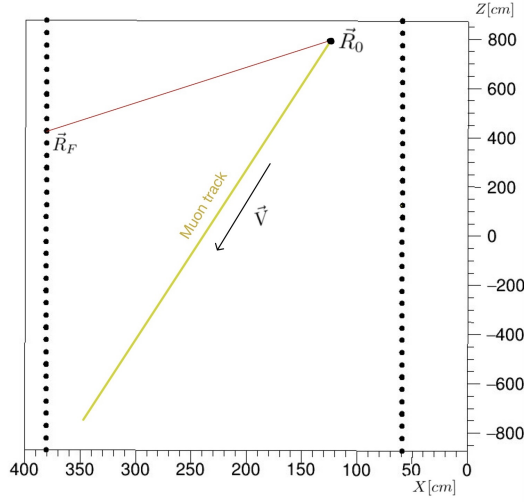


Figure 6.1: Optical Model in the case of $\ell = 0$

One of the perspectives to search for the initial position of the muon could be to start by finding its injection point through a preliminary χ^2 function that would have fewer parameters. If this approach is possible, we will perform a first χ^2 analysis with fewer parameters to find the value of t_{inj} , and, as a second step, we would continue with the search for the \vec{R}_0 value. From all the FHT recorded by the PMTs, the first FHT detected should be near the injection point of the muon. Suppose the photon with the lowest FHT travels from the muon injection point to a certain PMT. In this case, we do not need to consider the muon propagation time t_{muon} , Eq. (5.3). The photon's flight time is precisely the time that the photon travels from the injection point to the position, \vec{R}_F , of a certain PMT that captured the photon with the "First FHT" (FFHT) (see Figure 6.1),

$$t_{photon(F)} = \frac{|\vec{R}_F - \vec{R}_0|}{c/n_{LAr}}, \quad (6.1)$$

then the arrival time of the photon is simply

$$t_F = t_{inj} + \frac{|\vec{R}_F - \vec{R}_0|}{c/n_{LS}}, \quad (6.2)$$

which is a limit case of the model studied in Eq. (5.5), with $\ell = 0$ and considering the PMT position of the FFHT. In this particular case we eliminate four parameters, ℓ , and the three components of the unit vector \vec{V} . Therefore, this initial case depends on

$$T_F^{pre} = t_F(\vec{R}_F, \vec{R}_0, t_{inj}). \quad (6.3)$$

Compared with the complete χ^2 analysis of Eq. (5.1), which needs to consider all the PMTs positions that participate in the event, this last case only needs to consider the PMT position with the FFHT. Therefore, adding this first step would not be time-consuming. Minimizing first this new χ^2 is possible to find in advance the injection time t_{inj} and the injection point \vec{R}_0 . Once these values have been obtained, the complete analysis (Eq. 5.1) can be retaken, fixing t_{inj} and \vec{R}_0 , to find the direction of the muon \hat{V} .

Another possible improvement can be in the opposite direction, including more combinations of distances between PMTs and developing an algorithm to search for the minimum χ^2 along the known direction \vec{V} . To perform this type of analysis, the use of elaborated codes for χ^2 minimization, such as Minuit, may be indispensable.

Bibliography

- [1] S. Eidelman et al. Review of Particle Physics. *Physics Letters B*, 592:1+, 2004.
- [2] M. et al. Tanabashi. Review of particle physics. *Phys. Rev. D*, 98:030001, Aug 2018.
- [3] C. Adams et al. Rejecting cosmic background for exclusive charged current quasi elastic neutrino interaction studies with Liquid Argon TPCs; a case study with the MicroBooNE detector. *Eur. Phys. J. C*, 79(8):673, 2019.
- [4] Antonello et al. Icarus at fnal. 12 2013.
- [5] Gabriela Araujo. *Wavelength Shifting and Photon Detection of Scintillation Light from Liquid Argon*. PhD thesis, 03 2019.
- [6] Krishanu Majumdar and Konstantinos Mavrokoridis. Review of liquid argon detector technologies in the neutrino sector. *Applied Sciences*, 11(6), 2021.
- [7] P. B. (Palash B.) Pal. *An introductory course of particle physics / Palash B. Pal*. CRC Press, Boca Raton, FL, 2015 - 2015.
- [8] Donald Hill Perkins. *Introduction to high energy physics; 4th ed.* Cambridge Univ. Press, Cambridge, 2000.
- [9] Carl D. Anderson and Seth H. Neddermeyer. Cloud chamber observations of cosmic rays at 4300 meters elevation and near sea-level. *Phys. Rev.*, 50:263–271, Aug 1936.
- [10] Martin L. Perl. The Discovery of the tau lepton and the changes in elementary particle physics in forty years. *Phys. Perspect.*, 6:401–427, 2004.
- [11] R. I. Steinberg, K. Kwiatkowski, W. Maenhaut, and N. S. Wall. Experimental test of charge conservation and the stability of the electron. *Phys. Rev. D*, 12:2582–2586, Nov 1975.

- [12] Frederick Reines and Clyde L. Cowan. The neutrino. *Nature*, 178:446–449, 1956.
- [13] G. Danby, J. M. Gaillard, Konstantin A. Goulianos, L. M. Lederman, Nari B. Mistry, M. Schwartz, and J. Steinberger. Observation of High-Energy Neutrino Reactions and the Existence of Two Kinds of Neutrinos. *Phys. Rev. Lett.*, 9:36–44, 1962.
- [14] K. Kodama and N. et al. (DONUT Collaboration). Observation of tau neutrino interactions. *Physics Letters B*, 504(3):218–224, 2001.
- [15] Atsuto Suzuki and KamLand Collaboration. Results from KamLAND reactor neutrino detection. T121:33–38, jan 2005.
- [16] B. Pontecorvo. Neutrino Experiments and the Problem of Conservation of Leptonic Charge. *Soviet Journal of Experimental and Theoretical Physics*, 26:984, May 1968.
- [17] B. T. Cleveland, Timothy Daily, Raymond Davis, Jr., James R. Distel, Kenneth Lande, C. K. Lee, Paul S. Wildenhain, and Jack Ullman. Measurement of the solar electron neutrino flux with the Homestake chlorine detector. *Astrophys. J.*, 496:505–526, 1998.
- [18] Bruno Pontecorvo. Mesonium and antimesonium. *Zhur. Eksptl'. i Teoret. Fiz.*, 33, 1957.
- [19] Bruno Pontecorvo. Inverse *beta* processes and nonconservation of lepton charge. *Zhur. Eksptl'. i Teoret. Fiz.*, 34, 1958.
- [20] Shalom Eliezer and Arthur R. Swift. Experimental Consequences of electron Neutrino-Muon-neutrino Mixing in Neutrino Beams. *Nucl. Phys. B*, 105:45–51, 1976.
- [21] H. Fritsch and P. Minkowski. Vectorlike weak currents, massive neutrinos, and neutrino beam oscillations. *Physics Letters B*, 62(1):72–76, 1976.
- [22] S.M. Bilenky and B. Pontecorvo. Lepton mixing and neutrino oscillations. *Physics Reports*, 41(4):225–261, 1978.
- [23] Carlo Giunti and Chung W. Kim. *Fundamentals of Neutrino Physics and Astrophysics*. 2007.
- [24] S. Fukuda et al. (Super-Kamiokande Collaboration). Solar ^8B and hep neutrino measurements from 1258 days of super-kamiokande data. *Phys. Rev. Lett.*, 86:5651–5655, Jun 2001.

- [25] Ivan Esteban, M. C. Gonzalez-Garcia, Alvaro Hernandez-Cabezudo, Michele Maltoni, and Thomas Schwetz. Global analysis of three-flavour neutrino oscillations: synergies and tensions in the determination of θ_{23} , δ_{CP} , and the mass ordering. *JHEP*, 01:106, 2019.
- [26] A. Aguilar-Arevalo et al. Evidence for neutrino oscillations from the observation of $\bar{\nu}_e$ appearance in a $\bar{\nu}_\mu$ beam. *Phys. Rev. D*, 64:112007, 2001.
- [27] Pedro AN Machado, Ornella Palamara, and David W Schmitz. The Short-Baseline Neutrino Program at Fermilab. *Ann. Rev. Nucl. Part. Sci.*, 69:363–387, 2019.
- [28] A. A. Aguilar-Arevalo et al. Improved Search for $\bar{\nu}_\mu \rightarrow \bar{\nu}_e$ Oscillations in the MiniBooNE Experiment. *Phys. Rev. Lett.*, 110:161801, 2013.
- [29] A. A. Aguilar-Arevalo et al. Significant Excess of ElectronLike Events in the MiniBooNE Short-Baseline Neutrino Experiment. *Phys. Rev. Lett.*, 121(22):221801, 2018.
- [30] F. Kaether, W. Hampel, G. Heusser, J. Kiko, and T. Kirsten. Reanalysis of the gallex solar neutrino flux and source experiments. *Physics Letters B*, 685(1):47–54, 2010.
- [31] Joachim Kopp, Pedro A. N. Machado, Michele Maltoni, and Thomas Schwetz. Sterile Neutrino Oscillations: The Global Picture. *JHEP*, 05:050, 2013.
- [32] C. Rubbia. The Liquid Argon Time Projection Chamber: A New Concept for Neutrino Detectors. 5 1977.
- [33] K. N. Abazajian et al. Light Sterile Neutrinos: A White Paper. 4 2012.
- [34] C. Athanassopoulos et al. (LSND Collaboration). Evidence for $\bar{\nu}_\mu \rightarrow \bar{\nu}_e$ oscillations from the lsnd experiment at the los alamos meson physics facility. *Phys. Rev. Lett.*, 77:3082–3085, Oct 1996.
- [35] A. A. Aguilar-Arevalo et al. (MiniBooNE Collaboration). Event excess in the miniboone search for $\bar{\nu}_\mu \rightarrow \bar{\nu}_e$ oscillations. *Phys. Rev. Lett.*, 105:181801, Oct 2010.
- [36] A. A. Aguilar-Arevalo et al. (MiniBooNE Collaboration). Improved search for $\bar{\nu}_\mu \rightarrow \bar{\nu}_e$ oscillations in the miniboone experiment. *Phys. Rev. Lett.*, 110:161801, Apr 2013.

- [37] A.A. Aguilar-Arevalo, B.C. Brown, L. Bugel, G. Cheng, J.M. Conrad, R.L. Cooper, R. Dharmapalan, A. Diaz, Z. Djurcic, D.A. Finley, and et al. Significant excess of electronlike events in the miniboone short-baseline neutrino experiment. *Physical Review Letters*, 121(22), Nov 2018.
- [38] R. Acciarri et al. Design and Construction of the MicroBooNE Detector. *JINST*, 12(02):P02017, 2017.
- [39] Nicola McConkey and. SBND: Status of the fermilab short-baseline near detector. 888:012148, sep 2017.
- [40] D. Montanari et al. Development of membrane cryostats for large liquid argon neutrino detectors. *IOP Conf. Ser. Mater. Sci. Eng.*, 101(1):012049, 2015.
- [41] Dominic Brailsford. Physics Program of the Short-Baseline Near Detector. *J. Phys. Conf. Ser.*, 888(1):012186, 2017.
- [42] Jeff Eldred, Valeri Lebedev, Kiyomi Seiya, and Vladimir Shiltsev. Studies of beam intensity effects in fermilab booster synchrotron. 12 2020.
- [43] A. A. Aguilar-Arevalo et al. The Neutrino Flux prediction at MiniBooNE. *Phys. Rev. D*, 79:072002, 2009.
- [44] P. Adamson, K. Anderson, M. Andrews, R. Andrews, I. Anghel, D. Augustine, A. Aurisano, S. Avvakumov, D.S. Ayres, B. Baller, and et al. The numi neutrino beam. *Nuclear Instruments and Methods in Physics Research Section A: Accelerators, Spectrometers, Detectors and Associated Equipment*, 806:279–306, Jan 2016.
- [45] G. Charpak, D. Rahm, and H. Steiner. Some developments in the operation of multiwire proportional chambers. *Nucl. Instrum. Meth.*, 80:13–34, 1970.
- [46] S. Amerio et al. Design, construction and tests of the icarus t600 detector. *Nuclear Instruments and Methods in Physics Research Section A: Accelerators, Spectrometers, Detectors and Associated Equipment*, 527(3):329–410, 2004.
- [47] S. Amoruso et al. Analysis of the liquid argon purity in the ICARUS T600 TPC. *Nucl. Instrum. Meth. A*, 516:68–79, 2004.
- [48] B. Ali-Mohammadzadeh et al. Design and implementation of the new scintillation light detection system of ICARUS T600. *JINST*, 15(10):T10007, 2020.
- [49] E.L. Snider and G. Petrillo. LArSoft: toolkit for simulation, reconstruction and analysis of liquid argon TPC neutrino detectors. *Journal of Physics: Conference Series*, 898:042057, oct 2017.

- [50] Kun Zhang, Miao He, Weidong Li, and Jilei Xu. Muon tracking with the fastest light in the juno central detector. *Radiation Detection Technology and Methods*, 2(1), Mar 2018.